Titre: Title:	Toward a High-Throughput Device Able to Transport and Track Microscale Components Over Long Distances
Auteur: Author:	Louis Malosse
Date:	2023
Type:	Mémoire ou thèse / Dissertation or Thesis
Référence: Citation:	Malosse, L. (2023). Toward a High-Throughput Device Able to Transport and Track Microscale Components Over Long Distances [Master's thesis, Polytechnique Montréal]. PolyPublie. https://publications.polymtl.ca/55713/

POLYTECHNIQUE MONTRÉAL

affiliée à l'Université de Montréal

Toward a high-throughput device able to transport and track microscale components over long distances

LOUIS MALOSSE

Département de génie physique

Mémoire présenté en vue de l'obtention du diplôme de *Maîtrise ès sciences appliquées*

Génie physique

Août 2023

POLYTECHNIQUE MONTRÉAL

affiliée à l'Université de Montréal

Ce mémoire intitulé :

Toward a high-throughput device able to transport and track microscale components over long distances

présenté par **Louis MALOSSE**

en vue de l'obtention du diplôme de *Maîtrise ès sciences appliquées*

a été dûment accepté par le jury d'examen constitué de :

Clara SANTATO, présidente

Lucien WEISS, membre et directeur de recherche

Frédéric LEBLOND, membre

ACKNOWLEDGEMENTS

I would like to thank my research supervisor, Lucien Weiss, who has accompanied me throughout this year, giving me the benefit of his experience and giving me his time, which we don't know where he manages to find.

I would also like to thank all my colleagues for their invaluable help and their presence inside and outside the laboratory.

I would like to thank Elise, who kept me going every day on this project, and Antoine and Ben, who pushed me through the final days of writing.

Finally, I would like to thank my family, who have always supported me, even thousands of kilometers away.

RÉSUMÉ

Dans les laboratoires modernes, l'exigence d'intégrer rapidement et de manier avec précision des échantillons à l'échelle du micromètre a stimulé la création de technologies innovantes. Cette étude expose la conception et les résultats expérimentaux initiaux d'un appareil développé pour transporter et suivre des échantillons micrométriques sur de longues distances. En s'appuyant sur les principes de la microfluidique, ce dispositif vise à connecter différents appareils, permettant ainsi d'imager les mêmes échantillons avec divers équipements.

La solution suggérée consiste à déplacer les cellules d'un appareil à un autre à travers des tubes microfluidiques et à les suivre à l'aide d'un code-barres fluorescent. En insérant aléatoirement des billes entre les échantillons en transit, nous créons des séquences de fluorescence enregistrées sur les deux dispositifs connectés. Grâce à des algorithmes dérivés de ceux utilisés en bio-informatique pour aligner des séquences de nucléotides, il est possible d'aligner les séquences de fluorescence mesurées et ainsi de reconnaître et d'apparier les échantillons au fur et à mesure de leur passage sous chacun des dispositifs.

En exploitant les principes de l'écoulement des liquides à l'échelle micrométrique, cette étude cherche à démontrer la faisabilité de cette technologie et expose les défis à relever pour y parvenir. Dans ce travail, nous abordons les problèmes liés au transport des échantillons, à la mesure des séquences et au traitement informatique nécessaire pour suivre les échantillons en mouvement, tout en esquissant des orientations pour le futur développement de cet outil.

Les premiers résultats montrent qu'il est possible de suivre efficacement les échantillons, en supposant que les séquences de fluorescence restent stables pendant le transport entre les appareils. Les expériences suivantes explorent différentes méthodes pour concrétiser cette hypothèse, en manipulant les échantillons et les billes fluorescentes dans le flux pour tenter de les maintenir dans un ordre spécifique.

ABSTRACT

In modern laboratories, the need for seamless integration and precise manipulation of micrometer-scale samples has spurred the development of innovative technologies. This study presents the conceptualization and preliminary experimental results of a device designed to transport and track micrometer-sized samples over extended distances. By harnessing the principles of microfluidics, this device aims to bridge the gap between multiple apparatuses, enabling the imaging of the same samples across different devices.

The proposed solution involves moving cells from one device to the other via microfluidic tubing and tracking them using fluorescent flow barcoding. By randomly intercalating beads between samples in transit, we create fluorescence sequences recorded at each of the two connected devices. Using algorithms derived from nucleotide sequence alignment algorithms developed for bioinformatics, it is possible to align the measured fluorescence sequences and thus recognize and match the samples as they pass under either device.

By exploiting the principles of liquid flow at the micrometer scale, this study seeks to demonstrate the feasibility of such a technology and presents the challenges that need to be overcome to achieve it. In this work, we address the issues of sample transport, sequence measurement and the computer processing required to track flowing samples, and outline guidelines for the further development of this tool.

Initial results demonstrate that it is possible to track samples efficiently, assuming stable fluorescence sequences during transport between apparatuses. The rest of the experiments explore ways of making this hypothesis a reality, by manipulating samples and fluorescent beads in the flow in an attempt to keep them in order.

TABLE OF CONTENTS

LIST OF FIGURES

LISTE OF SYMBOLS AND ABBREVIATIONS

3D-IFC → 3D Imaging Flow Cytometer

ACF → Acoustic Contrast Factor

AFM → Atomic Force Microscopy

CLEM → Correlative Light and Electron Microscopy

CTC → Circulating Tumor Cells

DAPI → 4′,6-diamidino-2-phenylindole

DEP → Dielectrophoresis

EV → Extracellular Vesicles

FITC → Fluorescein Isothiocyanate

FOV → Field Of View

GFP → Green Fluorescent Particle

H&E → Hematoxylin and Eosin

MAP → Magnetophoresis

NWA → Needleman-Wunsch Algorithm

RBC → Red Blood Cells

SLA → Stereolithography

SMR → Suspended Microchannel Resonator

SNR → Signal-to-Noise Ratio

TDIRM → Time Delay Integration Readout Mode

WBC → White Blood Cells

LIST OF APPENDICES

CHAPTER 1 INTRODUCTION

While the development of optical microscopy techniques over the last few decades has enabled us to constantly reduce the scale of observable phenomena, improved resolution alone does not enable us to fully understand the underlying physical principles of biology. First, living organisms and the mechanisms that govern them are intrinsically dynamic, and so the integration of the temporal component in observations is essential. Second, it is essential to consider the heterogeneity inherent in cell populations, since this provides information that is indistinguishable from an integrated study of an entire population. Finally, the possibility of performing multiple measurements in different modalities enables us to collect a much richer dataset so that we can cross-reference and combine the observations.

While multimodal instruments exist, it is difficult to combine many disparate tools into a single device. An alternative way to achieve this is to create a system capable of moving and tracking individual cells over distances well in excess of the micrometer to carry cells between instruments. To link the data between different instruments, it is necessary to know when the same cell is being measured. We propose to do so using a microfluidic device and fluorescent bead-based barcoding, where objects in flow are used as barcodes that are read with an inexpensive imaging device so that the technology can be adapted to any laboratory or instrument facility.

1.1 Imaging modalities

Due to the requirements of measuring inside a microfluidic device, optical microscopy lends itself well to demonstrating multimodal methods and as a barcode readout. Of course, optical microscopy encompasses numerous techniques, some of which are described below. We focus on the modalities that are easiest to implement in our proposed flowing-cell system and could be implemented in serial. Indeed, each modality must overcome the two constraints imposed by flow-imaging, namely the ability to image cells that are in a microfluidic channel, on the other side of a wall, but also to acquire measurements quickly enough since the cells do not remain in the measurement zone for long.

1.1.1 Brightfield microscopy

A light source is positioned beneath the sample, and the light passes through the specimen. The sample absorbs some of the light, resulting in variations in brightness and darkness in the image.

These differences in light absorption generate contrast, allowing us to visualize the specimen's features [1]. Although brightfield microscopy is a label-free method, dyes can be used to discriminate cell components. For example, hematoxylin and eosin stain (H&E stain) can be used to enhance the contrast between certain cell structures by specifically absorbing certain wavelengths more than others. Traditionally, these labeling methods are not highly specific; hematoxylin binds to acidic compounds in the cell such as DNA and RNA, staining the nucleus, as well as certain structures and organelles (rough endoplasmic reticulum, ribosomes, collagen, myelin, etc.), elastic fibers and acidic mucins) with a violet hue, and eosin reads on the basic components of the cell (cytoplasm, connective tissues, and some extracellular matrix components) to tint them a pinkish-red color [2]. However, it is possible to target structures of interest more specifically via immunostaining, the operation of which is illustrated in Figure 1.6. Immunostaining can be used to bind an enzyme, a fluorophore, or a nanoparticle to the target (this is discussed in greater detail below Figure 1.6). The three markers have been used for brightfield microscopy [3] and it has been shown that data acquisition can be multiplexed over 12 different colors thanks to the use of molecules with sufficiently distinct spectra and hyperspectral acquisition [4].

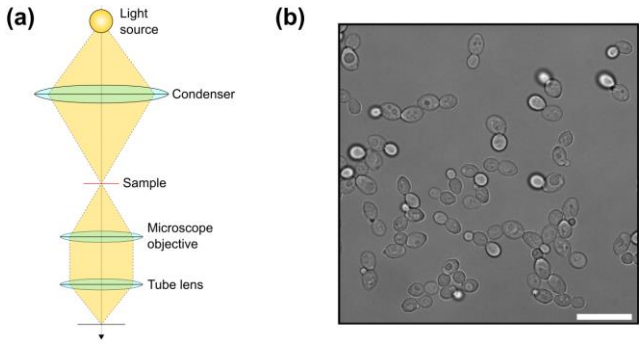

Figure 1.1 Brightfield microscopy: (a) Visible light is focused on the sample and absorbed by its structures (b) Unstained brightfield image, scalebar: 50µm [5]

Although this is an old technique, its simplicity and robustness make it still a widely used method today. Its limitations in terms of resolution stem from the diffraction of light by structures whose size is close to visible wavelengths (i.e., a few hundred nanometers).

In its simplest form, it is generally used to observe cell morphology [6], identify diseases or pathogens [5].

1.1.2 Darkfield microscopy

Darkfield microscopy operates on the principle of light scattering instead of light absorption. A specially angled light source is used to illuminate the sample from the side, causing light to scatter off structures and particles within the specimen. The scattered light is then captured by the objective lens, while the directly transmitted light is blocked. This results in a dark background, with the sample appearing bright against it, making it ideal for visualizing transparent or unstained specimens [7].

Similar in use to brightfield microscopy, darkfield is preferable for imaging highly transparent specimens and fine structures that scatter light better than they absorb it (cilia, flagella). Darkfield microscopy is also the preferred method for imaging labelled samples using scattering nanoparticles [8]. These are made visible by the scattering of incident light, and eliminating all directly transmitted light maximizes contrast.

There are several techniques for illuminating the sample to ensure that the objective only collects light scattered by the sample. The traditional technique is to use a mask on the illumination side to block the central part of the incident beam, so as to easily discriminate between direct and scattered light.

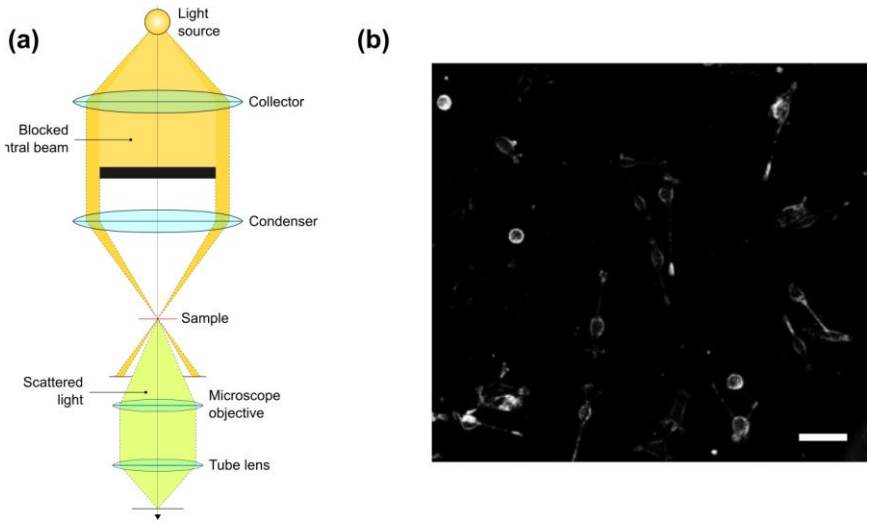

Figure 1.2 Darkfield microscopy: (a) Direct light is blocked from reaching the objective to collect only the scattered light, resulting in a dark background image like (b) scalebar: 50µm [9]

Since direct light arrives with a wide angle, it is easily discriminated against scattered light by a mask or simply by the lens' limited numerical aperture.

Another method, side illumination, uses a straightforward approach to discriminate between direct and indirect light. By using a light source orthogonal to the imaging system, direct light does not propagate towards the optics, and only scattered light is captured. What's more, this method lends itself well to the illumination of objects in a microfluidic chip.

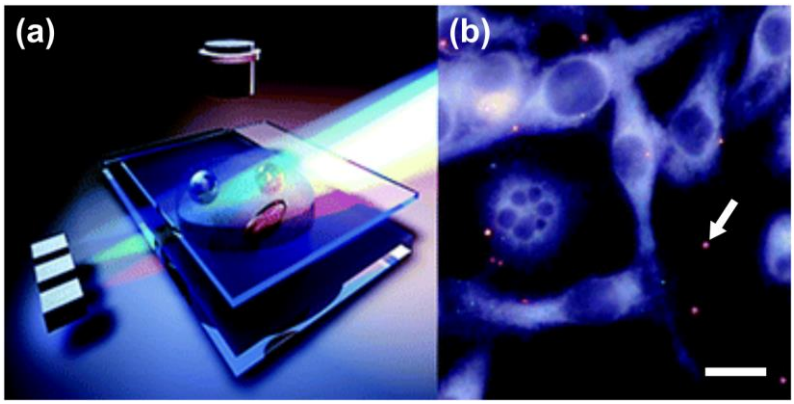

Figure 1.3 Side illumination darkfield microscopy [10]: (a) The light sources are on the left side, the objective is placed orthogonally above the glass slide to get an image like the one on (b) Arrows points to a nanoparticle, scalebar: 20µm

With this method, the authors achieve a better signal-to-noise ratio (SNR) than with the illumination method presented earlier.

1.1.3 Phase contrast microscopy

Phase contrast microscopy, invented by Frits Zernike in 1942 [11], uses direct radiation and radiation deflected by the specimen to maximize image contrast. Like the darkfield microscopy method shown in Figure 1.2, a phase contrast microscope blocks part of the incident light with a ring before focusing it on the specimen. As it passes through the specimen, the scattered light accumulates a phase delay of approximately $\pi/2$ which is not sufficient to create noticeable interference. The central idea of the phase contrast microscope is to use an annular phase mask in the back focal plane of the objective. Undeflected light, which still propagates in the shape of a ring, undergoes a phase shift of $\pi/2$ so as to be approximately in phase opposition with the light scattered by the specimen, which passes through the non-annular part of the phase mask [11]. Direct and scattered light are then almost in phase opposition, maximizing the contrast obtained by interference. The light path is shown in the following diagram:

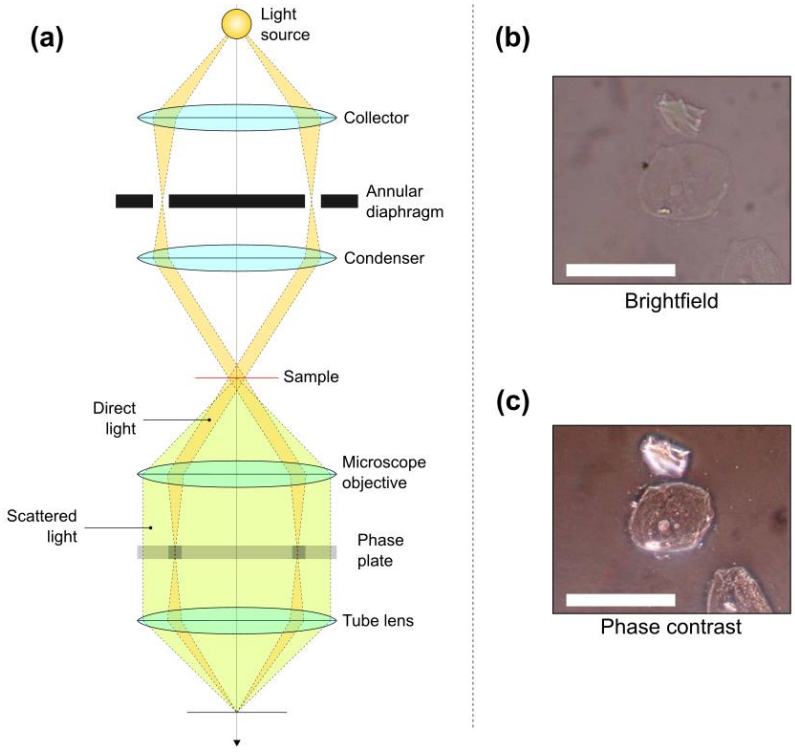

Figure 1.4 Phase contrast microscopy: (a) Direct light undergoes a $-\pi/2$ phase shift into the phase plate (dark grey areas) to hit the detector nearly in phase opposition with the scattered light, creating contrast from phase difference (b) and (c) phase contrast creates higher contrast than brightfield, scalebar: 20µm

The contrast formed on the screen is a function of the phase differences between direct and scattered light and is far superior to that of a similar image produced using brightfield microscopy. On the other hand, phase contrast microscopy produces a halo artifact near high-contrast structures, which can make dense images difficult to read. The cause of the halo effect is complex and will not be detailed here, but a mathematical derivation of its origin is detailed in the work of Nguyen et al. [12] who propose a method for online digital correction of this halo artifact.

1.1.4 Fluorescence microscopy

Fluorescence microscopy harnesses the phenomenon of fluorescence, where certain molecules, known as fluorophores, absorb light around a certain wavelength (excitation) and emit light around a longer wavelength (emission).

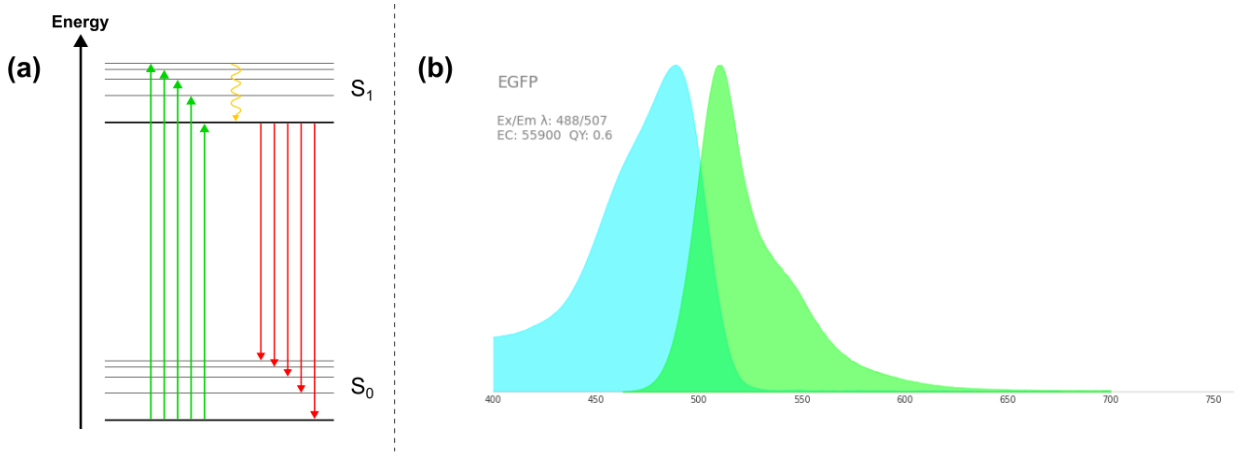

Figure 1.5 Fluorescence principle: (a) A Jablonski diagram represents the different energy transitions that a molecule can go through during a fluorescence process, resulting in (b) wide excitation/emission diagrams (here for GFP, Green Fluorescent Particle) [13]

There are several methods for labeling samples with fluorophores, the most common being immunostaining as described in Figure 1.6.

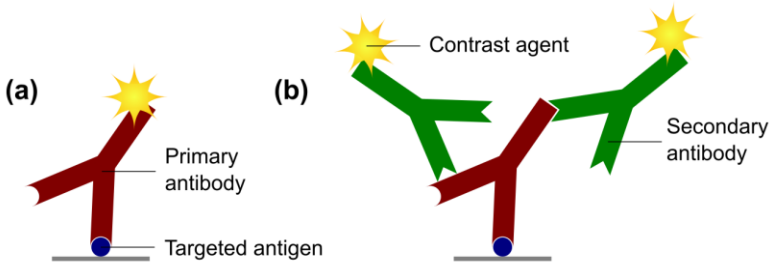

Figure 1.6 Principle of immunostaining: (a) a single antibody is used for direct immunostaining (b) a secondary antibody is linked to the primary antibody for indirect immunostaining.

A primary antibody selected to target an antigen of interest is attached to the target. In the case of direct immunostaining, the primary antibody also carries the contrast agent. For indirect immunostaining, a secondary antibody selected to bind to the primary antibody and carrying the contrast agent binds to the primary antibody. Indirect immunostaining is generally preferred to direct immunostaining as it amplifies the signal, since several secondary antibodies can bind to the primary antibody, thereby increasing signal intensity. The signal is produced by the contrast agent, which, in the case of fluorescence microscopy, is a fluorescent particle. These particles can be fluorophores, which are molecules able to absorb and reemit light as described in the Jablonski diagram above [14]. Fluorescent nanoparticles have also been used to create contrast using

fluorescent emission. Notable fluorescent nanoparticles include quantum dots, which are nanoscale semiconductor particles whose absorption and emission spectra depend on the size of the particle [15], making them a highly tunable and bright fluorescent markers. There are a tremendous number of types of fluorescent nanoparticles that behave in different ways and that are not going to be discussed in detail here but that are discussed with much detail in the work from Chandra et al. [16].

To image samples labeled with fluorophores, a fluorescence microscope relies on filters to discriminate wavelengths. The operating principle of a fluorescence microscope is illustrated in *Figure 1.7*.

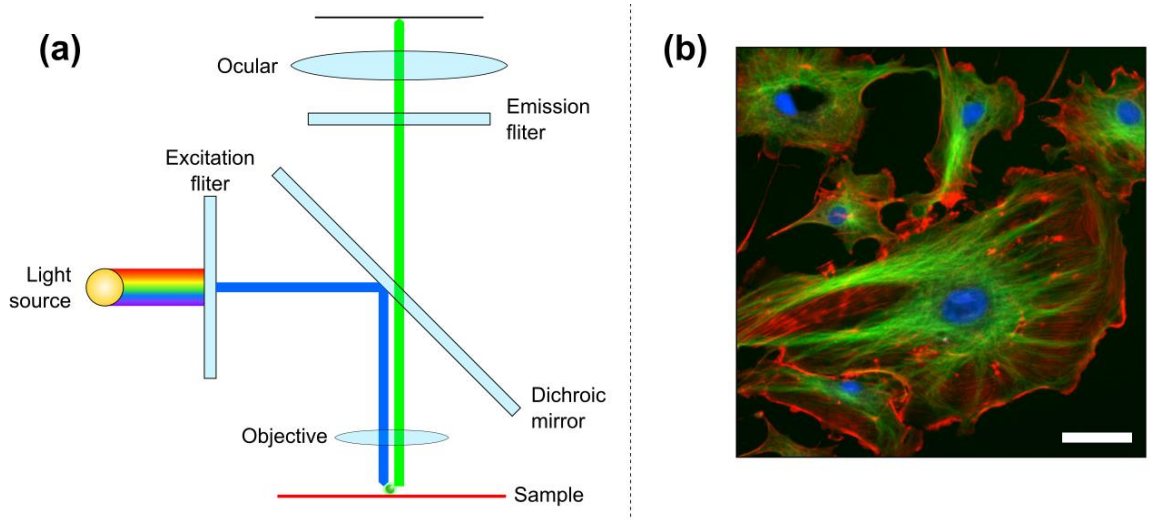

Figure 1.7 Fluorescence microscopy: (a) By filtering light depending on the wavelength, fluorescence microscopy allows for very low background (b) Fluorescent labeling and light filtering make it possible to discriminate different structures. Nuclei are stained with DAPI, microtubules are labeled green by FITC and actin filaments are marked red with phalloidin, scalebar: 20µm

The variety of fluorophores makes it possible to multiplex image acquisition in fluorescence microscopy, as long as the emission spectra of the fluorophores can be discriminated. This is clearly shown in Figure 1.7 where three different structures (nucleus, microtubules, and actin filaments) are imaged at the same time while being distinguishable by the color they are labeled with. Experiments have already demonstrated the simultaneous use of eight different fluorophores to label as many different structures [17] and simulated the possibility of ten fluorophores

simultaneously, enabling multimodal imaging as long as the component of interest can be fluorescently labeled.

The use of selective filters greatly reduces the background mainly generated by scattered illumination light but also autofluorescence of the sample, generating high contrast and making fluorescence microscopy a very sensitive modality such that even single-molecule fluorophores can be visualized above the background [18]. The labeling techniques employed are also highly specific. Finally, fluorophores are biocompatible, enabling the imaging of living cells.

Fluorescence microscopy encompasses a large number of different modalities based on the same use of fluorophores, but different illumination processes, the main difference being how the illumination and detected system are constructed. In flow imaging, light sheet illumination can be used for rapid 3D data acquisition. By focusing laser light in one plane, sections of a cell can be illuminated. As it passes through the sheet of light, the cell is scanned by the illumination, slice by slice. Simply place an objective lens on the axis orthogonal to the plane to capture images of the cell sections and reconstruct the 3D structure of the cell by computer. The process is described in Figure 1.8:

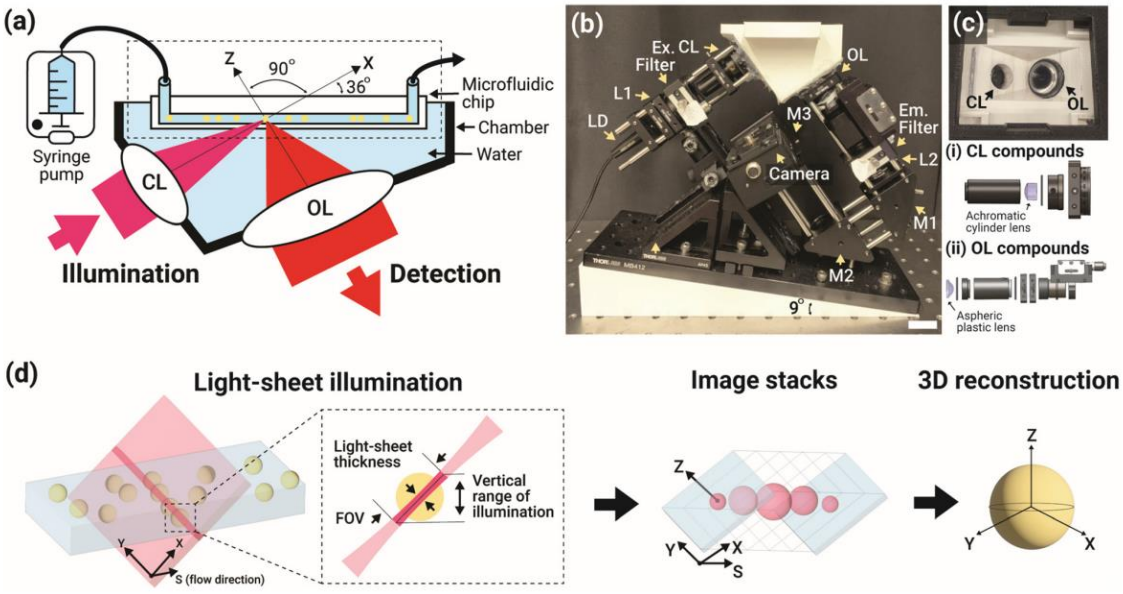

Figure 1.8 Light-sheet optofluidic device by Son et al. [19]: The cylindrical lens (CL) focuses the light-sheet at a 36° angle (wrt the flow), and the objective lens (OL) is set perpendicularly to collect the emitted light (b) Picture of the setup (LD, laser diode; L, lens, Ex, excitation; Em, emission; M, mirror), scale-bar: 25mm (c) Custom immersion chamber (d) Data acquisition and reconstruction pipeline

Irrespective of the method, fluorescence microscopy typically has two major shortcomings: phototoxicity and photobleaching; however, neither of these are very important for fast imaging.

1.2 Microfluidics

In addition to imaging modes, we also need a way to transport objects between our devices. Here we choose to deploy microfluidics, which is described briefly in this section.

1.2.1 Stokes flow

Liquid flows are characterized by the Reynolds number [20], which quantifies the ratio between inertial and viscous forces. It is given by equation (1.1):

$$Re = \frac{\rho U L}{\mu} \tag{1.1}$$

Where ρ is the density of the fluid, μ its dynamic viscosity, U its velocity and L the characteristic length of the flow. For water moving at 1mm/s in a microfluidic pipe of characteristic dimension 50µm at 20°C, we can estimate the Reynolds number at around 0.05. This is the Stokes regime ($Re \ll 1$), in which viscous forces dominate over inertial forces [21].

For steady-state flow of an incompressible fluid with no external forces, we can write the Navier-Stokes equation of momentum in simplified form:

$$\rho(\boldsymbol{u} \cdot \nabla \boldsymbol{u}) = -\nabla p + \mu \Delta \boldsymbol{u} \tag{1.2}$$

Noting U the characteristic velocity of the flow and L the characteristic distance of velocity variation, we can write the following approximations for the terms of equation (1.2):

$$\rho(\boldsymbol{u} \cdot \nabla \boldsymbol{u}) \sim \frac{\rho U^2}{L} \tag{1.3}$$

$$\mu \Delta \boldsymbol{u} \sim \frac{\mu U}{L^2} \tag{1.4}$$

The inertial term (equation (1.3)) is negligible compared to the viscosity term (equation (1.4)) if:

$$\frac{\rho U^2}{L} \ll \frac{\mu U}{L^2}$$
$$\frac{\rho U L}{\mu} \ll 1 \tag{1.5}$$

On the left is the Reynolds number as defined in equation (1.1). In such a regime, the Stokes equation provides a good description of liquid flows:

$$\mu \Delta \boldsymbol{u} = \nabla p \tag{1.6}$$

In this approximation, the momentum equation of the Navier-Stokes equations is linear, which has several immediate effects. The first is the possibility of obtaining an analytical solution for creeping flows. This enables velocity profiles to be predicted with ease and accuracy. The second is the spatial and temporal symmetry that characterizes creeping flows, giving them a behavior that differs from that observed on macroscopic scales, and enabling the realization of devices with varied effects.

This makes creeping flow a highly consistent and predictable tool for manipulating microscopic particles. These creeping flows are implemented in microfluidic devices consisting of very narrow channels, typically several tens of micrometers wide, thus minimizing the Reynolds number since it is directly proportional to the flow's characteristic dimension (1.6). Secondly, the geometry of the channels makes it possible to manipulate the flow passing through them and the particles floating in them.

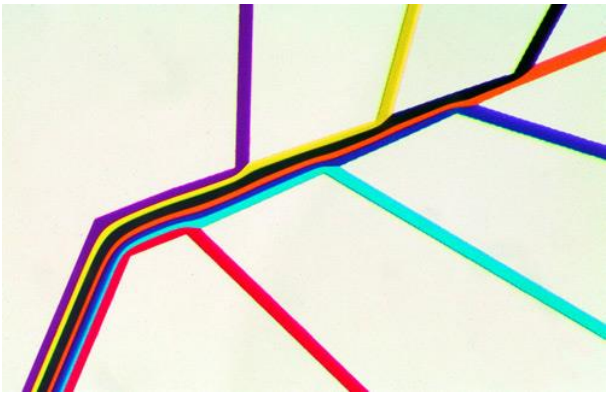

Figure 1.9 Flow within a microfluidic channel [22]. Fluid enters on the right and exits on the left. The streams meet but do not mix according to the laws of creeping flow.

Some of these geometries are presented later in 2.1.6 and in the following subsection.

1.2.2 Droplet generation

Plateau-Rayleigh theory describes why and how a fluid splits into droplets when stretched into a column. By splitting, the fluid retains its volume while reducing its surface area in contact with the

external environment, thus minimizing the energy caused by the surface interface [23]. On microfluidic scales, this phenomenon can be exploited to produce highly regular emulsions. Several geometries are possible, the main ones being described in Figure 1.10.

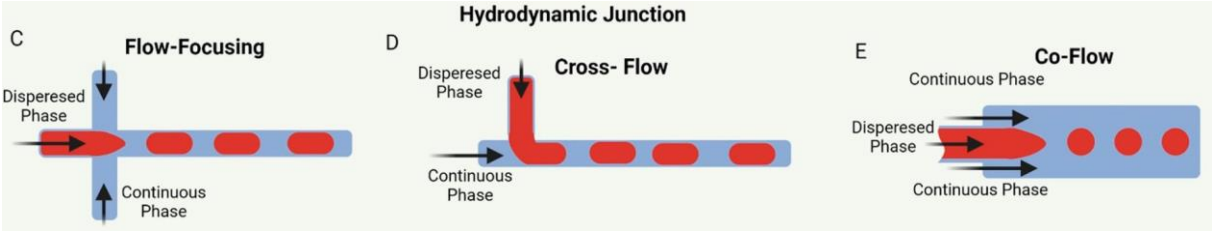

Figure 1.10 Diagram of different geometries utilized for droplet generation [24]

Several conditions must be met to produce a stable emulsion [25]. Firstly, the pipe walls must have a greater affinity to the continuous phase than to the dispersed phase. Secondly, the surface tension between the two phases must be sufficiently reduced so that the droplets do not fuse together. This is because two droplets that merge reduce the total surface area in contact with the medium, and will merge all the more easily the greater the surface tension between the phases [26].To reduce the surface tension between the phases, a surfactant can be diluted in one of the phases. In addition to influencing droplet stability, surfactant concentration also affects the size of droplets generated [26].

CHAPTER 2 LITERATURE REVIEW

In this section, we will summarize several key contributions from different authors that are relevant for this project. The next pages are organized around three components: microfluidics for cell manipulation, flow imaging and multimodal imaging.

First, we will discuss how microfluidic technologies have been used for single-cell manipulation, both to state how they are limited for long distance cell manipulation as is, but also how they could be used to achieve this project's goals. Then, we will review strategies that have been developed to overcome the hurdles set by flow imaging, as it requires to image objects that are flowing at high speeds (relatively to the size of the field of view and the imaging time) in an enclosed channel. These considerations will be essential to reach the highest possible throughput. Finally, we will detail how multimodal imaging unveils complex biophysical mechanisms and how it has been carried out at the single-cell level through several articles, and how complex and limited these methods can be.

2.1 Microfluidics for cell manipulation

2.1.1 Dielectrophoresis

Dielectrophoresis (DEP), invented by Pohl in 1951 [27], is a technique that exploits the electrical properties of cells to manipulate them with electric fields. When a polarizable particle, such as a cell, is immersed in an electric field, electric charges concentrate on its surface to counterbalance the external field. In a uniform field, charge clusters experience forces of equal intensity and opposite direction, resulting in equilibrium. When the field is non-uniform, the forces experienced by the cell's charges are no longer symmetrical, causing the cell to move towards areas where the field is strong or weak, depending on whether the cell is more or less polarizable than the medium in which it floats; this is the principle of DEP, schematized in *Figure 2.1*:

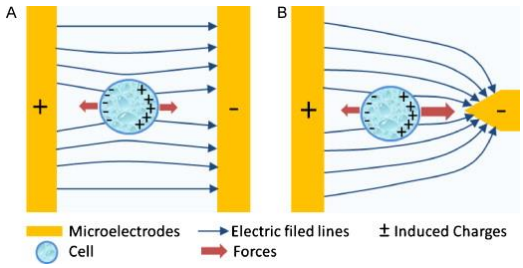

Figure 2.1 Dielectrophoresis principle: (A) A uniform electric field applies no force on a neutral, polarizable cell (B) When the field is non uniform, the resulting electrical force becomes non-zero for a polarizable cell [28]

DEP enables cells to be manipulated in a microfluidic device. In their 2022 work, Junwang et al. [29] separate RBCs from the plasma containing them by subjecting them to an AC electric field as they pass through a microchannel. Deported to the sides, the RBCs are then collected in lateral outlets, reaching 98.8% of extracted RBCs. DEP can also be used to discriminate between cells on the basis of inhomogeneities in their electrical characteristics. For these reasons, DEP is often used for the separation of circulating tumor cells (CTCs) from blood samples, for the purpose of diagnosis or in-depth study of cancer cells. By combining DEP with magnetophoresis (MAP), Thu et al. [30] were able to discriminate and isolate four cell types in a blood sample: CTCs, white blood cells (WBCs), platelets and RBCs with efficiencies of 93%, 96%, 94% and 52% respectively.

In order to create non-uniform fields with great precision at the scales imposed by microfluidics, electrodes are finely manufactured using techniques specific to microfabrication: photolithography, deposition (sputtering, evaporation or electroplating), ion etching, etc. [31].

2.1.2 Magnetophoresis

Operating on a similar principle to DEP, magnetophoresis (MAP) uses the magnetic properties of particles to manipulate them using external magnetic fields. Although some works present the use of MAP to exploit the intrinsic magnetic properties of cells (joint use of DEP and MAP by Thu et al. [30] presented previously), this technique is generally employed to manipulate cells to which superparamagnetic nanoparticles have been bound. Superparamagnetic nanoparticles have high magnetic susceptibility, but unlike ferromagnetic materials, they lose their magnetization once the external field is removed. This phenomenon is due to thermal fluctuations which, at this size scale, are large enough to randomly fluctuate the magnetic moment of nanoparticles [32].

Once the nanoparticles are attached to the cells of interest, they can be moved by the magnetic field. The work of Bakhshi et al. [33] illustrates the combination of hydrodynamic forces and magnetophoresis to separate CTC cells from a blood sample. To bind the nanoparticles to the CTCs, Bakhshi et al. let them incubate together for an hour before including the cancer cells in a blood sample. It is possible, however, to target markers with greater specificity directly in the blood sample containing the CTCs using nanoparticles functionalized with antibodies [34].

2.1.3 Optical trapping

Since their invention in 1986 by Arthur Ashkin [35], optical tweezers have found numerous applications in many fields of physics and biology. They work by focusing a laser beam on microscopic particles. The gradient in intensity of the beam creates forces that trap particles at the focus. If particles move away, scattering and refraction push them back, allowing them to trap and move particles by moving the focus point. These capabilities make optical tweezers a powerful tool for the precise manipulation of cells in a microfluidic device.

In an article published in 2020, Luro et al. [36] present the combination of a microfluidic device and optical tweezers to individually collect bacteria of interest after supervising their growth.

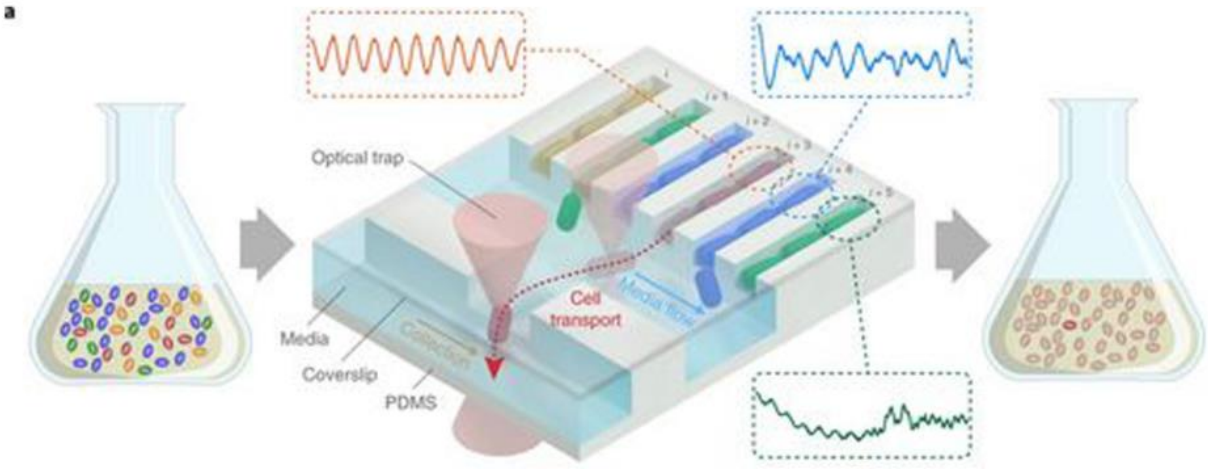

Figure 2.2 Optical trapping within a microfluidic device: The system proposed by Luro et al. [36] uses optical tweezers to move bacteria of interest from culture trenches to a collection channel

Using optical tweezers, the authors are able to select cells of interest and deposit them in a collection channel leading directly into a collection vessel. Total control over the cells is counterbalanced by a rather low throughput and the need to actively control the optical tweezers;

unlike the methods described above, which can be described as passive once the electromagnetic fields have been set up, the movements of the optical tweezers must be constantly and precisely supervised.

In their work, Yao et al. [37] use optical tweezers to trap RBCs in a microfluidic flow. By measuring the deformation of RBCs generated by drag forces, they are able to discriminate healthy cells, which are more elastic, from diseased cells, which are less so.

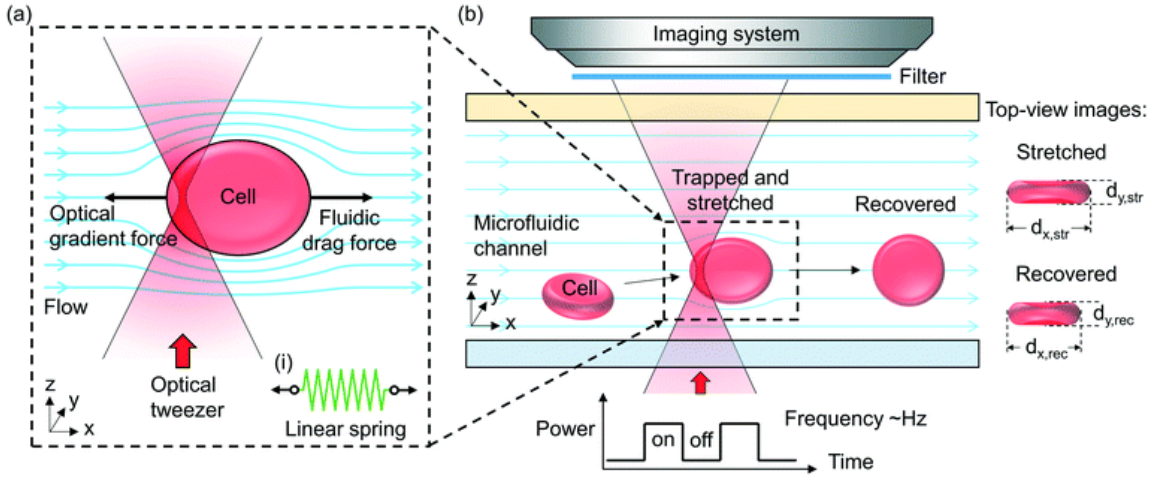

Figure 2.3 Tweeze-and-drag principle [37] (a) The RBC is trapped in place by the optical tweezer and dragged by the current, causing deformation approximated by (i) a linear spring (b) The optical tweezers trap and release RBCs while an imaging system registers their elongation

The tweezers flash at a frequency of the order of one Hz, limiting the technology's throughput but not requiring constant supervision.

2.1.4 Acoustic manipulation

Acoustic manipulation employs sound waves generated by piezoelectric transducers to create intricate pressure fields within microfluidic channels. These fields exert forces on particles and fluids, enabling their manipulation and precise positioning. Depending on its acoustic properties, a particle immersed in a non-uniform pressure field undergoes a force towards pressure maxima or minima.

This property can be exploited for acoustic focusing. By vibrating piezoelectric transducers at the right frequency, it is possible to generate a standing wave in a microfluidic channel. Particles, such as cells, are then concentrated towards the nodes or antinodes of the standing wave, ending up concentrated on a single current line. In their work, Piyasena et al. [38] successfully implement

multi-node acoustic focusing flow cells, in which the cells flowing down a glass capillary are organized into parallel streams (up to 37) that are simpler to image, with the aim of parallelizing flow cytometers to increase their throughput.

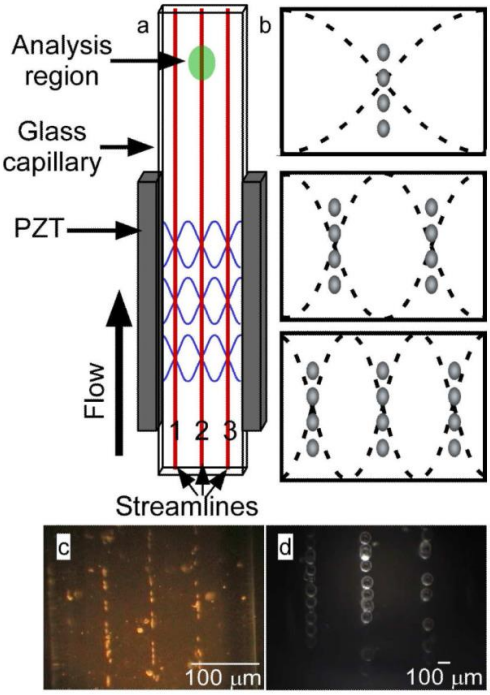

Figure 2.4 Multi-node acoustic focusing [38]: By selecting the resonance mode of the cavity, the authors can create an according number of acoustically focused streamlines

The control offered by acoustics can be more precise and individual than in the case of flow focusing; all that's needed is more precise control over the pressure field. By creating a custom piezoelectric transducer, Baudoin et al. [39] have succeeded in creating an acoustic tweezer that is similar in every respect to its optical counterpart.

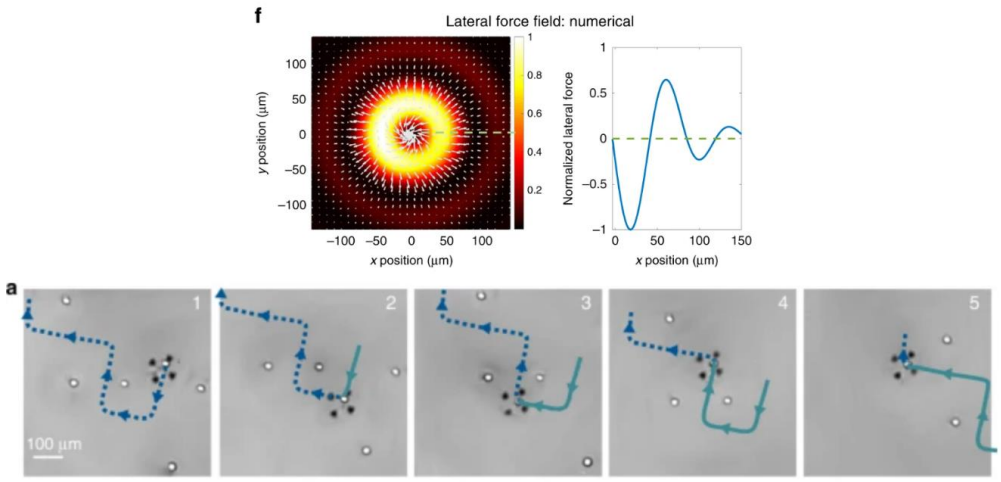

Figure 2.5 Acoustic tweezers capacities: (f) Force field of the tweezer, (a) Trajectory of a displaced cell (green arrow = past, blue arrow = future) [39]

This tweezer enables confinement forces two orders of magnitude above optical tweezers at equal intensity, without altering the integrity of the displaced cells. However, the trap's encroachment is much greater than that of an optical tweezer.

Acoustic manipulation offers the ability to precisely control the position of particles in the flow, however acoustic wave propagation in a microfluidic device is a complex phenomenon and the design of such systems requires a large investment in numerical simulations [40].

2.1.5 Hydrodynamic manipulation

All the techniques that go by the name of hydrodynamic manipulation exploit the passive properties of microfluidic flows. One strategy, employed by Patel et al. [41] and employed by most commercial flow cytometers, consists in using a sheath fluid introduced at the sides of the flow to focus the particle flow at the center of the channel. Sheath fluids are regularly used in conjunction with other methods since its implementation is relatively simple; this was the case in articles described above that employ it alongside dielectrophoresis [29] or magnetophoresis [32] for cell separation.

Another passive use of microfluidic flow properties is inertial focusing. By exploiting the density differences between the medium and the cells, and the size and density differences between the cells, it is possible to manipulate the cells passively by tuning the pipe geometry. In this way, it is possible to separate cells in a blood sample; using two devices, one coil-shaped and the other spiral-

shaped, Abdulla et al. [42] were able to separate four cell types (RBCs, WBCs, A-549 and MCF-7) on the basis of size differences. Inertial flow focusing and sheath fluid can be used together to separate CTCs from blood samples with an efficiency of 91% and a purity of 74%. [43].

2.1.6 Microfabricated structures

The flexibility of manufacturing microfluidic components using techniques such as soft lithography means that all kinds of structures can be included to interact with the cells in the flow. A simple method is to place obstacles in the path of the cells to trap them. A passive method is proposed by Lu et al. [44] described in *Figure 2.6*.

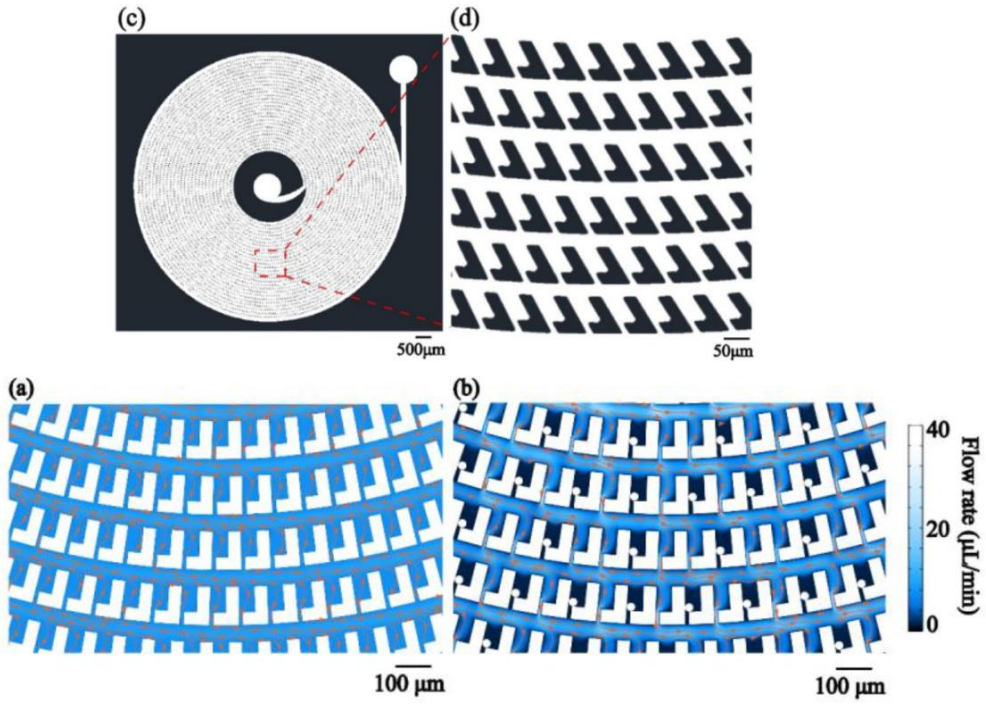

Figure 2.6 Dentate Spiral microfluidic channel trapping [44] : (c) general design and (d) close-up view of one of the serrated blocks, (a) streamlines and medium flow without and (b) with trapped cells.

Cells travelling along the anticlockwise spiral have a non-zero probability of being absorbed by a trap and remaining trapped there, thereby blocking the currents that would attract other cells into the same trap to maximize the probability of a single cell per trap.

Other methods use active trap techniques, as in the article by Nikoloff et al. [45] where the cells, after being stopped by pillars installed in the middle of the flow, are trapped using a system of valves capable of isolating the cells from the rest of the system. It is then possible to selectively

expose the cell or not to different flows that would be passed through the system to interact with the cell and its microenvironment, in this case to label and image the extracellular vesicles (EV) released by the cell.

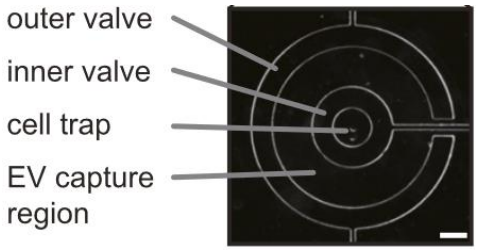

Figure 2.7 Valve isolation trap [45]: the flow of cells takes place over the whole image, and some cells are caught in the cell trap (center). The valves can then be operated to successively isolate the cell or its microenvironment.

2.2 Flow imaging

Flow imaging offers several advantages for cell imaging. Firstly, it enables high imaging throughput since the cells are constantly renewed in front of the objective. Secondly, it enables single-cell analysis since cells can be passed in front of the objective one by one. These two criteria are the cornerstones of flow cytometry, which enables quantitative analysis of cell populations, one cell at a time. However, imaging cells that are being transported in a flow, and therefore translating very rapidly in front of the objective, presents new constraints. Standard flow cytometers, which analyze thousands of cells per second, use point detectors to rapidly characterize large cell populations. These point detectors, generally photomultiplier tubes or avalanche photodiodes, enable very fast measurements thanks to their high sampling frequency, but completely miss all the degrees of freedom provided by an image.

The first constraint for imaging flowing cells is focus. Unlike cells on a flat support, cells in a liquid flow are not necessarily all in the same plane. To overcome this problem, the solution commonly employed is flow focusing. This can be achieved by employing (1) sheath fluid focusing, using an hydrodynamically focused stream of sheath fluid to align and confine cells or particles in a narrow single file [41] or (2) acoustic flow focusing, which involves using acoustic forces generated by a piezoelectric actuator to precisely align and concentrate cells or particles within a sample stream [46]. In addition to concentrating all cells in the focal plane of the imaging device, these methods allow cells to pass through the imaging section one by one.

The second constraint is motion blur. To overcome this, some cameras have a time delay integration readout mode (TDIRM), which is described in detail here:

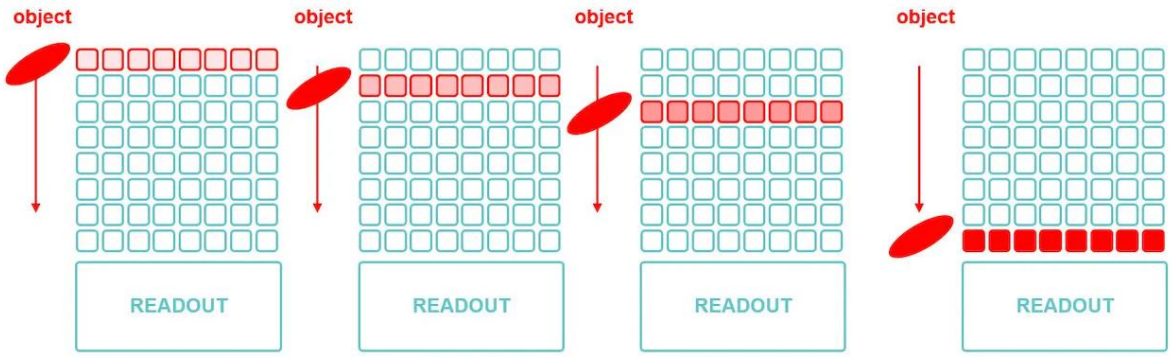

Figure 2.8 TDIRM principle [47]: The signal generated by incident photons is moved across the camera in sync with the moving object to continue the acquisition

Other methods use mirrors to ensure that the optical path follows the moving sample as it passes through the imaging section. This is the case with the polygon scanner (Figure 2.9) or similar methods based on galvonometers [48], [49].

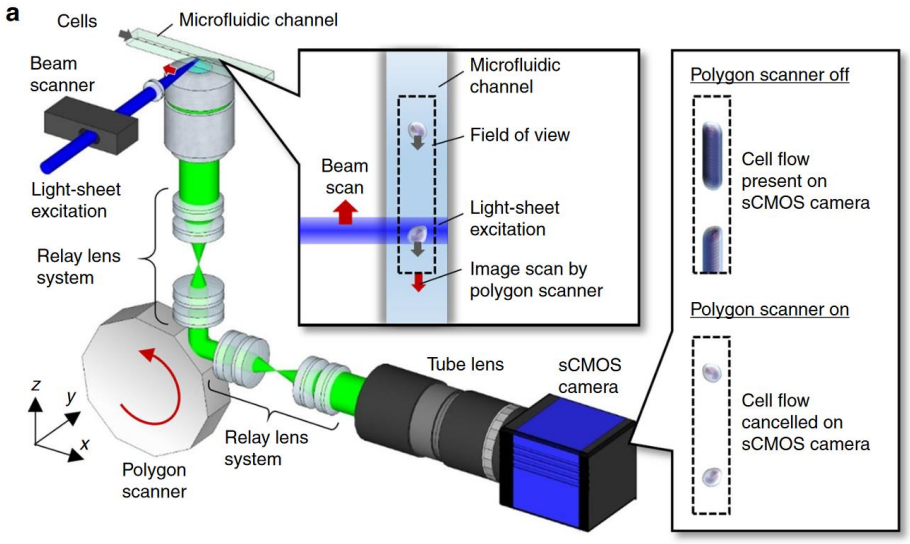

Figure 2.9 Virtually freezing flowing samples by beam scanning [50]

An additional constraint caused by imaging flowing fluorescent objects concerns intercellular quantitative analysis. A constant illumination time is essential if the signal intensity has an importance for the analysis, so the samples need to be flown at the same rate as it passes in front of the camera.

2.3 Fluorescent barcoding

Like the macroscopic barcodes we deal with every day, microscopic barcodes are used to mark an object (say, a cell) for later identification. When an experiment becomes more complex, i.e. the number of motile cells increases or they are not imaged during a long period of time, it is no longer possible to track them individually using basic optical microscopy tracking, and barcodes are needed to retrieve information at the level of the individual cell. There are several methods for creating microbarcodes, as shown in Figure 2.10 :

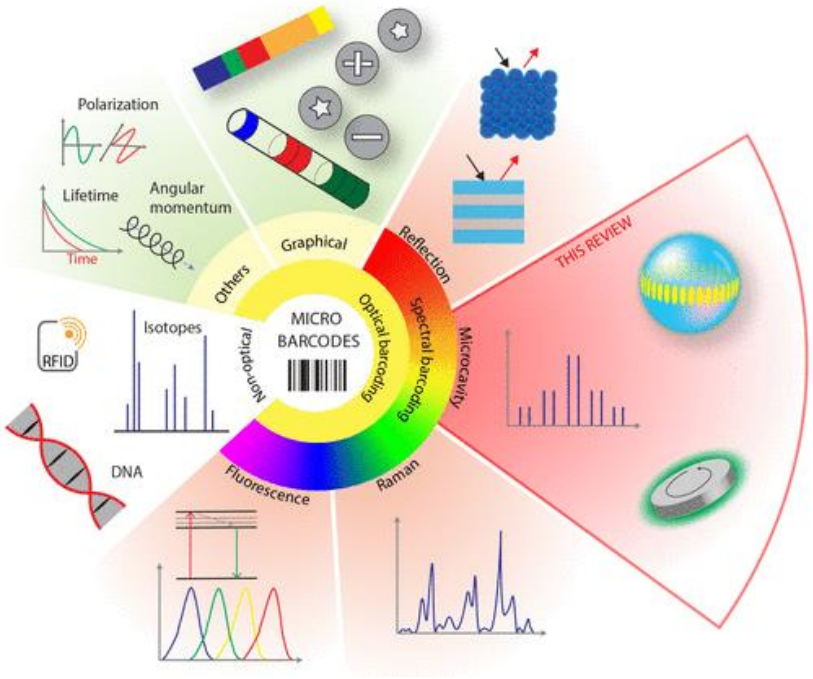

Figure 2.10 Different barcoding modalities [51]. The mention "This review" in the microcavities section is specific to the article from which the figure is taken and is not related to this report.

In this section, we review barcoding methods using fluorescence.

The challenge imposed by barcoding is to make as many distinct codes as possible. A fluorescence microscope is limited by its ability to distinguish the emission spectra of the fluorescent dyes used to create the barcode. In practice, as we saw earlier, it is very difficult to distinguish more than eight fluorescent emitters [17], which limits the usefulness of a naive barcode. Adding to the complexity and number of distinct codes available thus generally involves the use of combinatorics or fluorescent intensity ratios between wavelengths. In their 2005 paper, Li et al. [52] use DNA probes attached to a variable number of fluorescent dyes to mark beads.

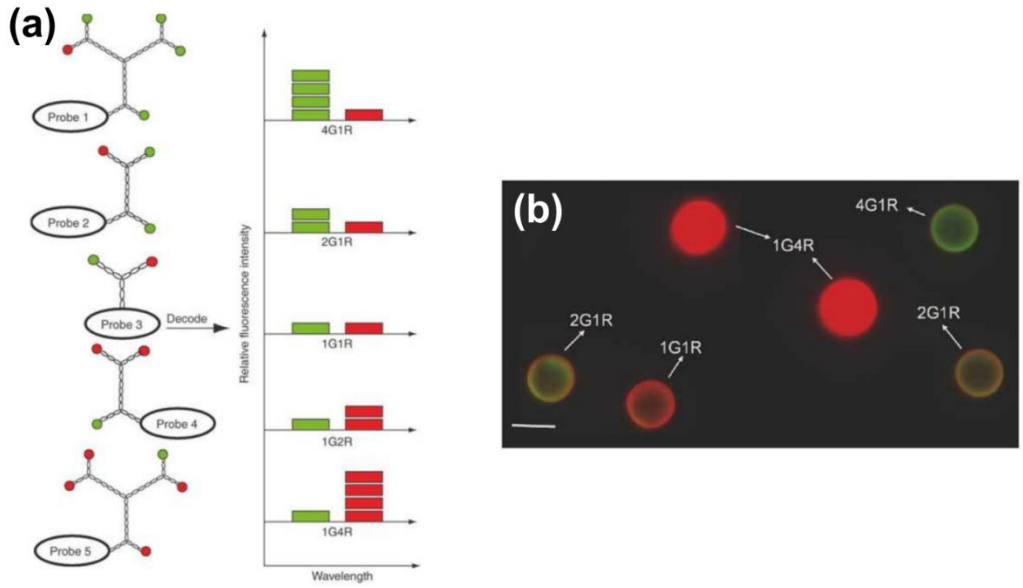

Figure 2.11 Intensity ratios to characterize the marker (a) Several DNA molecules carrying different dye ratios are attached to beads, (b) beads can be recognized using quantitative intensity ratios between the red and green wavelengths.

By using just two colorants, it is possible to distinguish a greater number of codes. The beads can then be linked with the object to be marked.

Using a similar strategy, the work of Feng et al [53] presents a technique for creating fluorescent beads from lanthanides in solution. Lanthanides are elements with fine, distinguishable fluorescent spectra, and are distributed in controlled proportions in hydrogel beads. Once created, the beads are imaged on 9 channels of distinct wavelengths, and the brightness ratios between the 9 channels are used to discriminate the different bead groups. Using this technique, another team from the same group has shown that it is possible to discriminate over 1100 distinct codes, thus enabling as many cell groups to be marked and tracked [54].

In another paper, Lin et al. [55] use labeled nanorods to increase the complexity of the signal using three colors. The nanorods are labeled on three different sites, and the order and color of the dyes enables to distinguish up to 30 different codes:

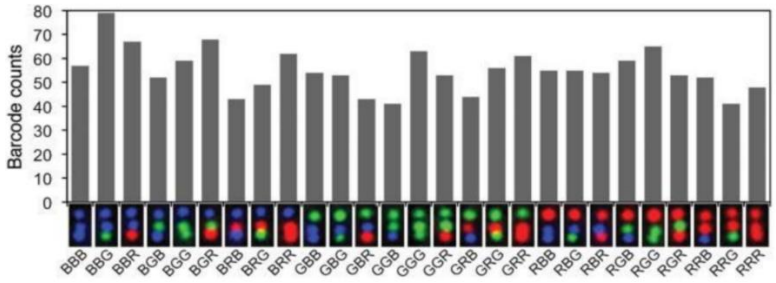

Figure 2.12 Spatial barcodes generated by the nanorods. The order of the R, G and B allow to distinguish more single codes

By shifting to super resolution methods and being able to distinguish mor than three points on the nanorod, it is possible to dramatically increase the number of codes available. The authors were able to create a nanorod with more binding sites, reaching the possibility of generating 823,543 different barcodes.

Finally, the idea of using combinatory information to increase the complexity of the code was used in a similar way in the 2022 article from Zhang et al. [56], where the space between flowing cells was involved to store the barcode. Three different types of beads are stochastically intercalated between flowing cells, forming sequences that are measured while the beads and cells are flowing in a flow cytometer. After the beads and cells exit the flow cytometer, they are placed in the same order on a platform where the sequences can be read again and algorithmically aligned, allowing the authors to track the cells between the cytometer and the platform:

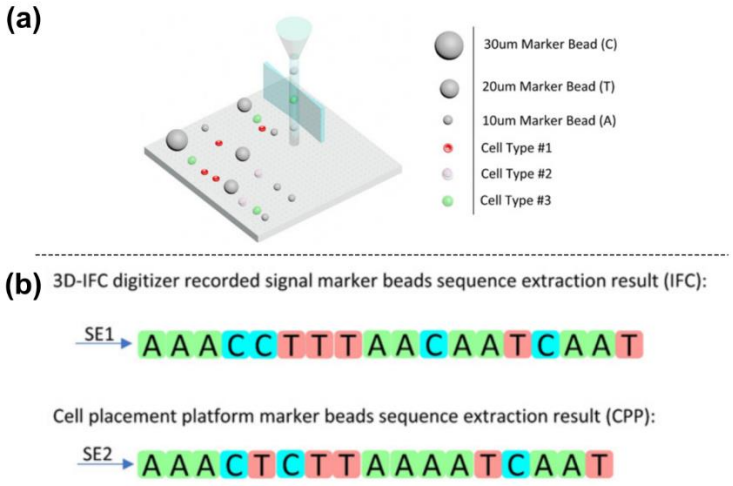

Figure 2.13 Sequential barcoding uses space between flowing objects (a) Sequences of beads and cells are measured as they flow in the cytometer, and are dropped on a cell placement platform, (b) The sequences act barcodes and can be aligned.

2.4 Multimodal imaging

Multimodal imaging involves using several imaging modalities on the same sample to cross-reference the results. As each modality reveals information that is sometimes inaccessible to other modalities, multimodal imaging makes it possible to establish correlations that would be impossible to obtain via a single measurement. Certain methods are known to yield complementary results, such as the joint use of fluorescence microscopy and electron microscopy in correlative light and electron microscopy (CLEM). While electron microscopy brings very high resolution to the images produced, fluorescence microscopy brings a high degree of specificity. [57], [58]. Same goes with fluorescence microscopy and atomic force microscopy (AFM), bearing numerous and otherwise inaccessible results [59], [60].

Although practicing AFM and CLEM in a microfluidic flow is hardly conceivable, it has been shown that microfluidics lends itself well to several modalities, particularly in light microscopy: imaging [61], [62], fluorescence microscopy [63], [64], Raman spectroscopy [65], [66] and mass spectrometry [67].

The use of multimodal measurements with microfluidics and imaging is generally part of the cross-study of omics and cell phenotypes at the individual level. This was the case in a study by Zhang et al. [68] which cross-references the results of observations of cell phenotype using fluorescence microscopy images, with cell genotype. Once the images have been taken, the cells are stored in a microwell array and marked with microbeads so that they can be recognized during the subsequent RNA-seq.

In another study, Altemose et al. [69] use high-resolution confocal microscopy to localize the sites of histone modifications in the cell. By combining these results with data obtained by sequencing the observed cells, the authors were able to search for correlations between DNA and the regulations that constitute and maintain the epigenome.

There are other studies crossing optical imaging or mass spectrometry results with sequencing technologies integrated into microfluidic devices, always with the aim of conducting genotype-phenotype correlative studies [70]–[73].

Other works present the multimodal study of samples at single-cell precision with optical tools that enable both cell characterization and manipulation. In their article, Luro et al. [36] move bacteria

of interest, whose growth in a microfluidic chip has been supervised, into a collection channel to isolate them for further measurements. Similarly, Zhang et al. [56] are able to link images produced in a custom 3D imaging flow cytometer (3D-IFC) to the cells that produced them, once these have been deposited on a placement platform from which they can be observed again. The Zhang et al. strategy is based on Needleman and Wunsch's algorithm for matching sequences of cells and microbeads observed in the flow cytometer to those deposited on the platform. This approach, similar to the one we are proposing, does not allow cells to be transported over long distances, however, since the cells are deposited on the platform a few millimeters after being observed in the flow-cytometer.

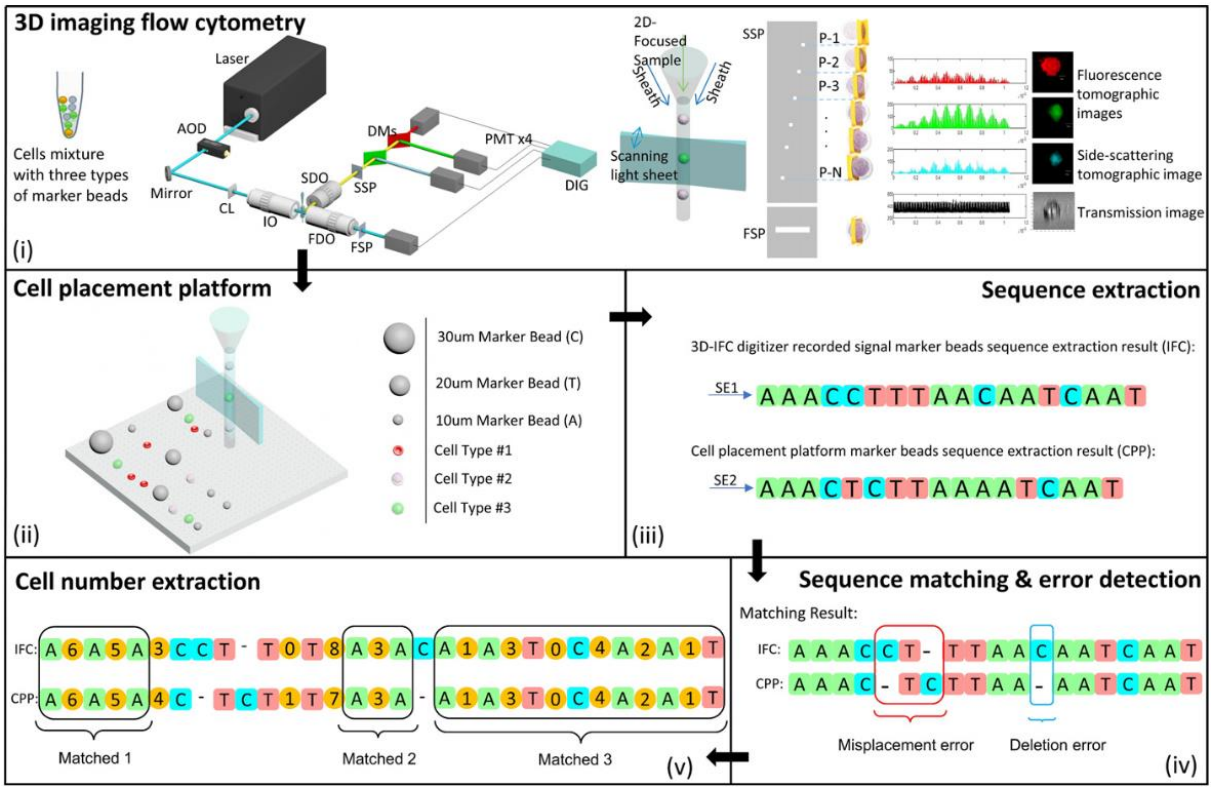

Figure 2.14 Cell pairing pipeline [19]: (i) Three types of marker beads are mixed with the cells and sent through the 3D-IFC (ii) Cells are placed on the platform as they come out of the 3D-IFC (iii) Sequences are extracted from the 3D-IFC and platform measurements (iv) Sequences are matched using the Needleman-Wunsch algorithm (v) Matching cell sights are paired

Other groups, such as Cermak et al. [74] have been able to displace and track cells between several measurements taken by different suspended microchannel resonators (SMRs) that vibrate according to the mass of the cell that passes by them. In order to evaluate the individual growth rate of a group of cells, the authors move them in microfluidic channels between measurements,

waiting for them to grow, for 4 to 20 minutes interspersed with numerous measurements. To keep track of the cells, they use a probabilistic approach with the assumption that the growth rate remains mostly constant and try to find the best match using the Hungarian algorithm [75].

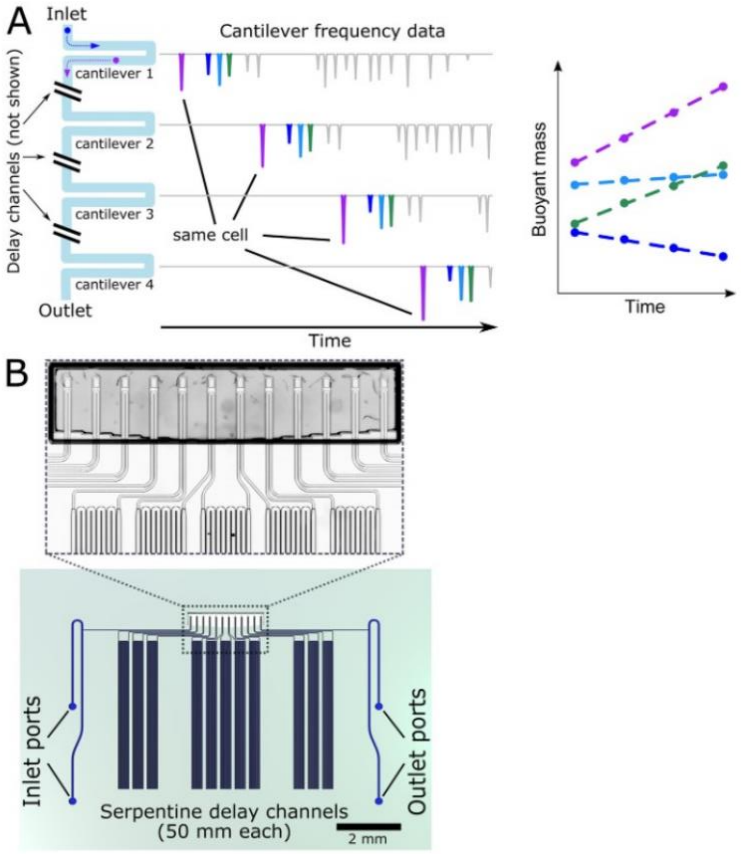

Figure 2.15 Design of the serial SMR array [20]: (A) Peaks that come from the same cells are matched and buoyant mass is deduced (B) Layout of the device showing the delay channels and vibrating cantilevers

One way of increasing the throughput of a flow imaging device is to tag the cells, so that they can be distinguished even at high density. One way of achieving this is through single-cell encapsulation, in which a cell and a fluorescent microbead are enclosed in the same droplet. It is then necessary to be able to discriminate as many groups as possible, and thus as many beads as possible. In their work, Feng et al. [53] develop a technique for marking and encoding samples with beads that carry a spectral and magnetic code. The spectral information is generated during the creation of the beads, in which different proportions of lanthanides (which have fine, easily resolvable luminescence) are incorporated. Another team from the same laboratory has demonstrated that this technique can create over 1100 distinct codes [54]thus enabling 1100

different groups to be marked. To achieve this, the beads are imaged on 9 channels of distinct wavelengths, and the brightness ratios between the 9 channels are used to discriminate the different bead groups. While this is practical for a flow cytometer, for imaging, splitting the light signal into 9 different channels is challenging and costly, and the limit of 1100 groups may be difficult to achieve under imaging conditions reduced by flow imaging.

What remains to be done is a device that can characterize samples over very long distances, keeping track of each induvial sample with a high throughput. A device of this kind makes it possible to link different imaging modalities together, or to perform time-lapse imaging by matching images taken of samples at different points in space and/or time, all at the single-cell scale. While microfluidic devices excel in precise manipulation on the microscale, scaling up to longer distances introduces several complexities that are discussed in the next parts of this report.

CHAPTER 3 METHODOLOGY AND RESULTS

This project involves building a device capable of transporting and tracking microscopic samples over macroscopic distances. To achieve this, we are introducing the Flow Barcoding technique, which involves placing samples in a microfluidic conduit that connects the two points separated by a long distance, while randomly intercalating markers (fluorescent beads) in the flow between the samples:

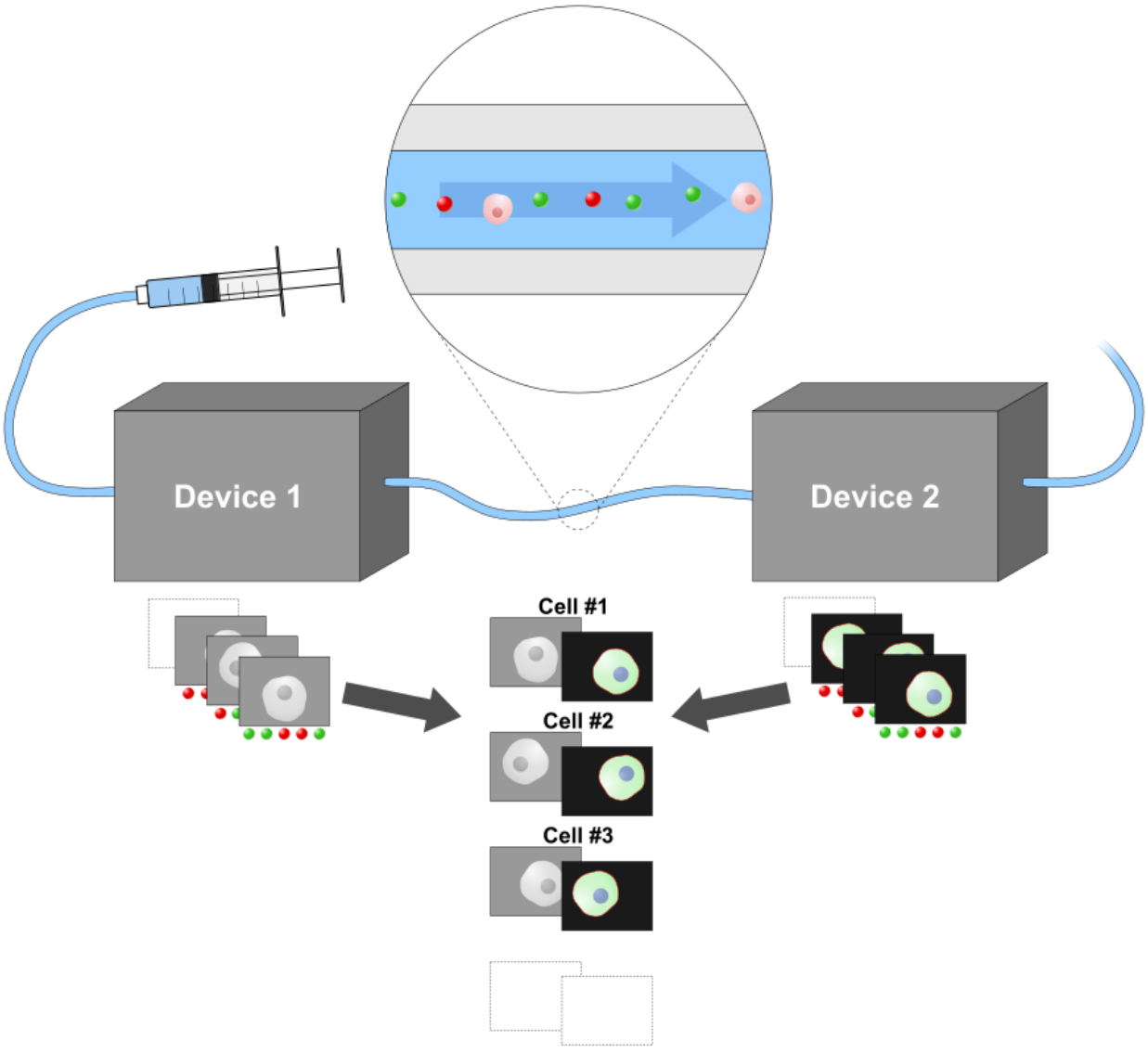

Figure 3.1 Working principle of the flow barcoding device: Two devices record different images of cells that can be matched thanks to the bead barcode intercalated between the cells.

Such a system measures a series of objects twice, one after the other, carrying information via the order in which they are arranged. A sequence is any succession of objects (beads and samples), real or measured.

The overall objective of this research is to create the device shown in figure 3.1, with consists of having two or more devices linked together that capture cellular data in different modalities that can be linked back to the same cell. To achieve this, it is necessary to be able to (1) Move microscopic samples over distances of several centimeters, (2) Detect and record sequences of beads and cells flowing through the device, (3) Match different measurements of identical objects using the information given by the sequences. Each of these objectives is broken down into sub-objectives that we will explore in the following chapter before finally commenting on the remaining barriers that must be overcome before achieving the goal. The sub-aims are:

(1) Moving microscopic samples
    a. Create a system of tubes and channels to move samples and image them in the flow.
    b. Servocontrol several pumps to control the flow and movement of objects in the system.
    c. Maintain the sequences' order as stable as possible when moving them between measurements.
(2) Detect and record sequences
    a. Set up a microscope to illuminate the beads and measure their fluorescence.
    b. Record and process the light signals detected at high-throughput.
(3) Match different measurements of identical objects
    a. Establish an algorithm for aligning sequences of objects of any length.
    b. Evaluate the algorithm's capabilities with degraded sequences.

3.1 Algorithms can match measured sequences

3.1.1 Adapting the Needleman-Wunsch algorithm

The Needleman-Wunsch algorithm (NWA) was developed in 1970 [76] to compare nucleotide sequences by finding similarities between them via identical sections. Given two bead sequences, the algorithm calculates the alignment that maximizes a previously established score function. Three scores are associated with the three possible configurations: A match, a mismatch, or a gap. Each of these configurations contributes to the overall score of a sequence alignment.

The optimal alignment of two sequences takes the following form:

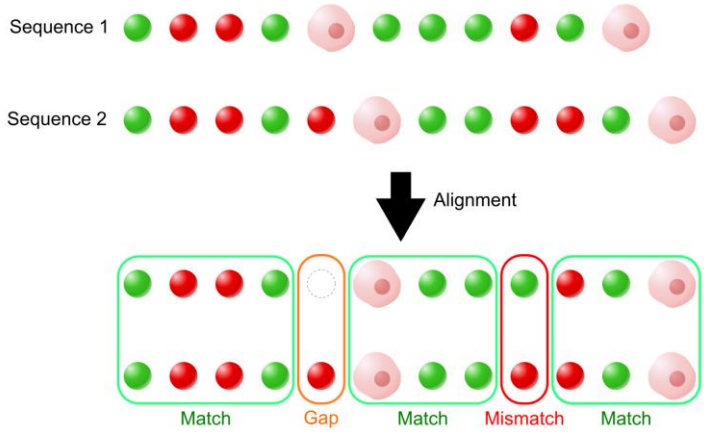

Figure 3.2 An alignment consists in pairing every element from one sequence to either an element of the other sequence or a gap, without swapping the order of the elements. The NWA finds the alignment that maximizes a predefined score function.

The previous alignment, which consists mainly in the position chosen for the gaps, is the one that maximizes the cumulative score of each of the pairings with the following scores: Match Score of 2, Mismatch Score of -3 and Gap Score of -2.

To find the alignment that maximizes the score, the algorithm relies on the systematic filling of a matrix of size NxM, where N and M are the respective lengths of the two sequences. We implemented and modified the basic algorithm on MATLAB.

In the case of our problem, we are measuring two sequences of objects at two points in space, which we know to be "theoretically" identical. In a system where all objects move at the same speed and none of them get stuck, we would measure two identical sequences that could be perfectly matched with the NWA, enabling us to recognize all objects individually at the different points where they were observed.

The NWA can be easily adapted to align any variety of "keys"; in its original usage, a key is a nucleotide, and here it will be a colored bead or a cell. The first thing to determine is the number of bead colors required minimize the possible alignment errors. To do so, let us consider two random sequences that separate two cells each, and then estimate the probability that they are identical. For this, we assume that the sequences are generated according to a binomial probability, which means that the next object in the sequence is randomly chosen according to its relative concentration. A short calculation (given in appendix) brings the following result:

$$P = \frac{n_{colors}}{n_{colors}(R+1)^2 - R^2} \tag{3.1}$$

With n_{colors} the number of different bead colors and R the ratio of beads over cells concentrations. Figure 3.3 illustrates this probability as the number of colors and the relative concentration of beads increase. It is important to note that we are not specifically concerned about having consecutive identical sequences, this is done only to give an estimation of the number of identical cell-to-cell sequences in a arbitrarily long global sequence.

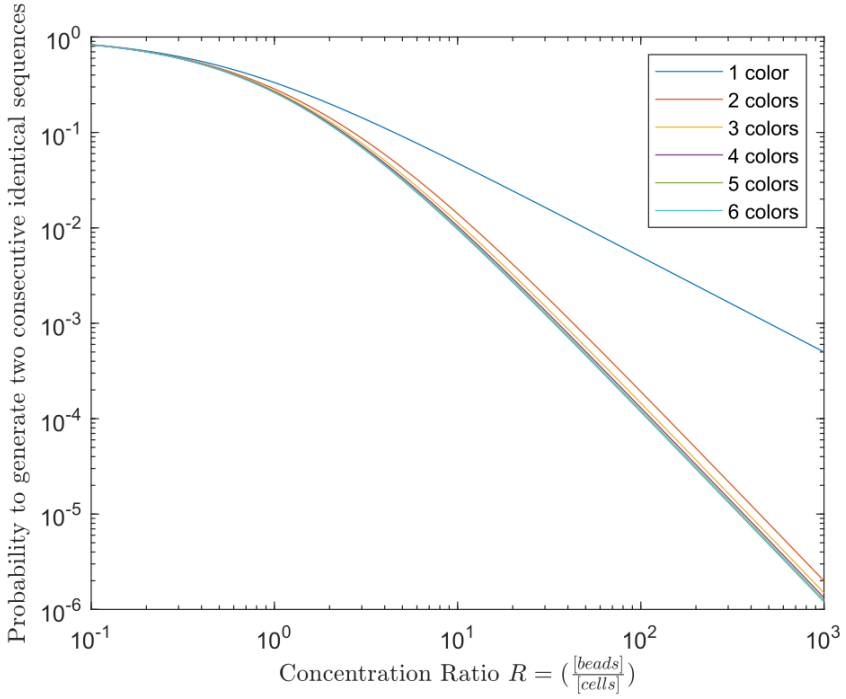

Figure 3.3 Probability to generate two consecutive identical sequences scales down with the concentration ratio and the number of colors, with a massive step from one to two colors.

Minimizing the probability of generating two identical sequences between two cells allows the algorithm to minimize mismatches. With this derivation, we observe that going beyond two bead colors only slightly reduces this probability, which has several advantages for the design of the detection system. In fact, each additional color of fluorescent bead requires a different excitation wavelength and must be discriminated from the other colors by different filters (see section on set-up).

However, there are still several major problems: the first is the systematic filling of the matrix, which makes this algorithm of complexity $O(n^2)$, making it unusable as is for very long sequences.

Second is that the algorithm doesn't integrate any temporal dimension data, which would presumably contain a significant amount of information, and finally, it does not deal well with bead inversions.

The first problem can be solved relatively easily by subdividing the problem into sub-problems with short sequences (detailed in the next section). The second is more inherent to the algorithm's operation and involves characterizing the algorithm's robustness to the errors that a real system would incorporate in the sequences. To do this, we simulate two phenomena: the interchanging of different beads according to a probability that models the inhomogeneity of speeds in the conduit, and errors in reading the detection system. We simulate the degradation of many sequences and match the two sequences measured at different points:

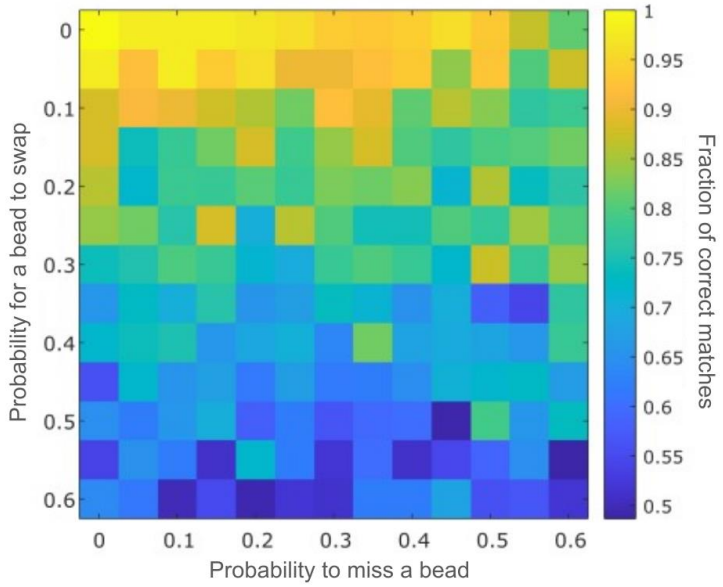

Figure 3.4 NWA capacity to overcome missed beads and swapped beads.

As described earlier, "missed" beads are not a problem for being able to align sequences (Make another figure that measures gradients to prove that the slope is much greater on the vertical axis than horizontal?). On the other hand, bead reversals are a major barrier to the success of the algorithm, whose performance drops sharply as the probability of reversal increases. A major challenge for this project is therefore to maintain the sequences in the best possible condition for as long as possible.

The second problem, namely that the complexity grows as the square of sequence length, can be solved by dividing sequences into sub-sequences of "reasonable" length (i.e., matchable in realistic time).

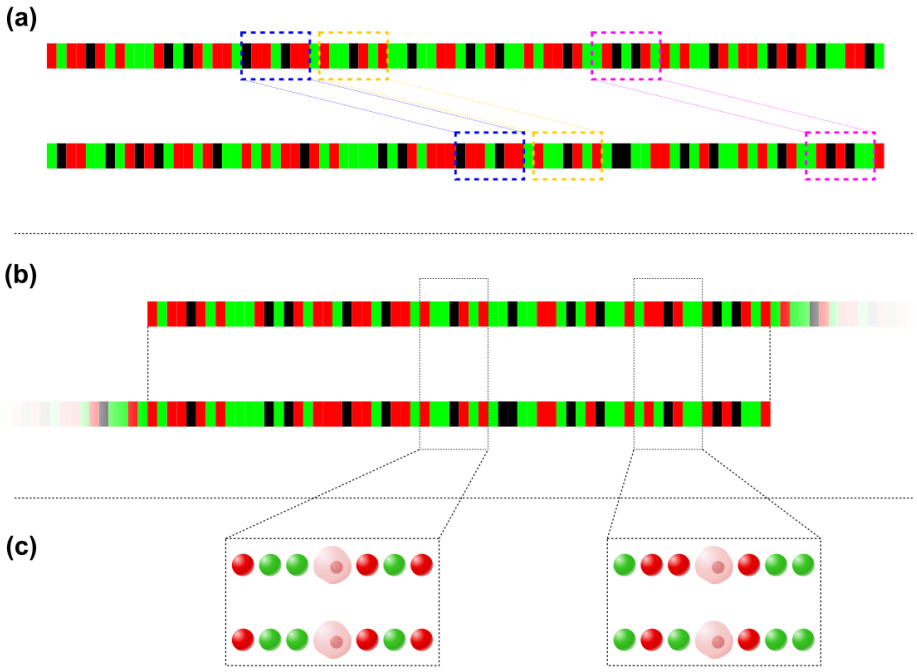

Figure 3.5 Dividing alignment of long sequences into computable problems: (a) Random short sequences of the first sequence are aligned with the second sequence (b) Sequences are globally aligned (c) Short sequences are locally aligned around objects of interest.

This strategy can be recursively applied to deal with any size of sequence.

3.2 Implementation of an experimental system

The experimental system built must have the sensitivity to detect individual objects, and the ability to discern their different types. In this experimental project, the objects are 10μm diameter fluorescent beads, which are representative of the size of the samples this project aims to manipulate.

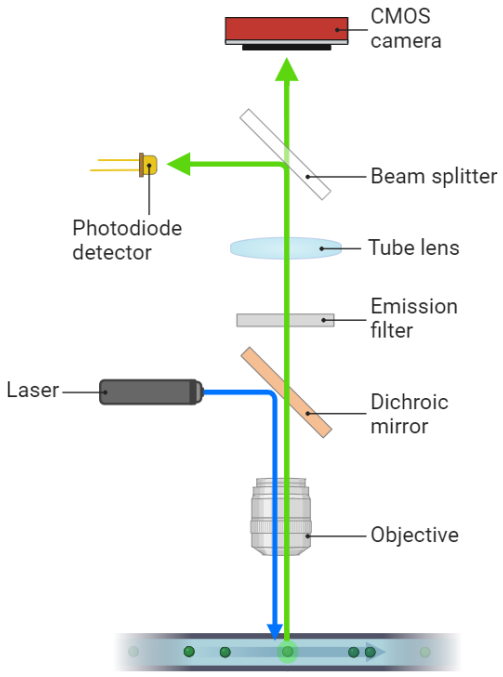

Figure 3.6 A diagram of the experimental setup to measure fluorescence bead sequences.

This is a basic fluorescence microscope in which the collected fluorescence is separated between a CMOS camera and a photodiode-based detector. The high light intensity generated by bead fluorescence means that detectors such as photodiodes are compact, simple, fast (potentially in the MHz range) and inexpensive. By separating the wavelengths appropriately, a functional system with photodiodes would return the nature and instant of detection of each object, making it possible to establish the sequences required for matching. The camera, which is more complex, less compact, much more expensive and capable of a lower sampling speed (<100Hz), nevertheless enables us to study the behavior of objects in the duct with information that the photodiode cannot provide. The goal is to dispense with cameras altogether.

The various experiments presented in this work required different magnifications and thus different objectives, without the rear part of the device being profoundly changed.

3.3 Calibrating the detectors

In theory, the bright intensity of fluorescent beads would enable the use of low-cost point detectors, namely photodiodes, to be used. This has the advantages of cost, processing simplicity, and sampling rate. The low cost also would enable the system to be easily implemented many times over a length of tube.

3.3.1 Methodology

Photodiode detectors require calibration for fluorescent bead detection, and their sampling speed is characterized to estimate the maximum flow rate achievable in the microfluidic channel for desired high flow rates. The limiting factor for data acquisition speed is the USB interface between the Arduino Uno R3 board and the photodiode's analog signal.

By utilizing MATLAB in conjunction with the Arduino IDE, we determined that the highest achievable sampling speed via a computer is 4kHz. To enhance the sampling rate, we transitioned the system to a Raspberry Pi nano-computer, which doesn't rely on USB connections. Instead, it employs GPIO pins capable of acquiring binary signals. This shift increases the sampling rate, and binary signal poses no issue for sequencing.

With a USB interface, the sampling rate peaks at 4kHz. However, utilizing the Raspberry Pi's GPIO interface, the sampling rate surpasses 10MHz.

To correlate the detector's signal with camera observations, we employed the setup detailed in Figure 3.6. Fluorescent beads are pumped into the microfluidic conduit before pumping ceases, reducing their movement for optimal signal observation when a bead enters the camera's field of view.

3.3.2 Limitations

In practice, the detectors we have been building were unusable in the lab environment as they were picking too much electrical noise for any relevant signal to be read. We built rudimentary Faraday cages with no success.

3.4 Measuring the flow profile

3.4.1 Choosing the beads and medium

As beads are loaded in a syringe pump without mixing, we chose to create a solution that matches the beads density to avoid buoyancy effects, so the bead solution can remain homogeneous during the experiment. The polystyrene beads being less dense than water, ethanol (density of 0.789 at room temperature) was chosen to be mixed with water in order to get a lighter solution. After diluting a 95% ethanol solution in a bead+water solution, the samples were centrifugated to

separate the beads from the solution. The right ethanol concentration was found to be 5% (v/v), which corresponds to a bead density of 0.989.

This 5% ethanol solution was used as the carrying medium for beads during the whole project.

3.4.2 Preliminary test with flowing micro-scale objects

Several pumps can be used to flow liquids inside micro-channels.

While some peristaltic pumps can deliver flow rates as low as 7µL/min, commonly found ones; including the one in our possession; can not reach flow rates as low as that. A flow rate too high makes it impossible to image flowing beads. With an exposure time of 10ms, and the dimensions of the channel used to image the beads (300x300µm²), a flow rate of 60µL/min is the maximum acceptable flowrate (calculation derived in the Annexe). This value is not met by our peristaltic equipment. While this is a problem if a CMOS camera is involved, a system without any camera could withstand higher flow rates, hence use a peristaltic pump.

The experiments for this project were conducted using ESSI.tech syringe pumps. They can reach flow rates as low as 0.001µL/min when using the appropriate syringe (the flow depends on the motor speed and the syringe diameter), and they can be precisely controlled through a USB UART which is identical to some Arduino boards. The pumps were supervised using the Arduino serial monitor and MATLAB.

The connexion between the pumps and the glass square channel in which the beads were imaged was ensured by 500µm inner radius silicone tubing. The interfaces between the glass channel and the tube were carried out by shoving the channel in the tube and sealing the connexion.

3.4.3 Data acquisition

By flowing a highly diluted fluorescent bead solution inside a square channel (300x300µm²), we were able to measure the speed of the objects inside of the channel relatively to their position in the channel. To simplify the computation of the acquired data, the laser was strobed, and the camera exposure time was set to be a multiple of the strobing period of the laser. This enables to get several sights of the same bead on the same image, and to compute its speed easily. The process is given by Figure 3.7:

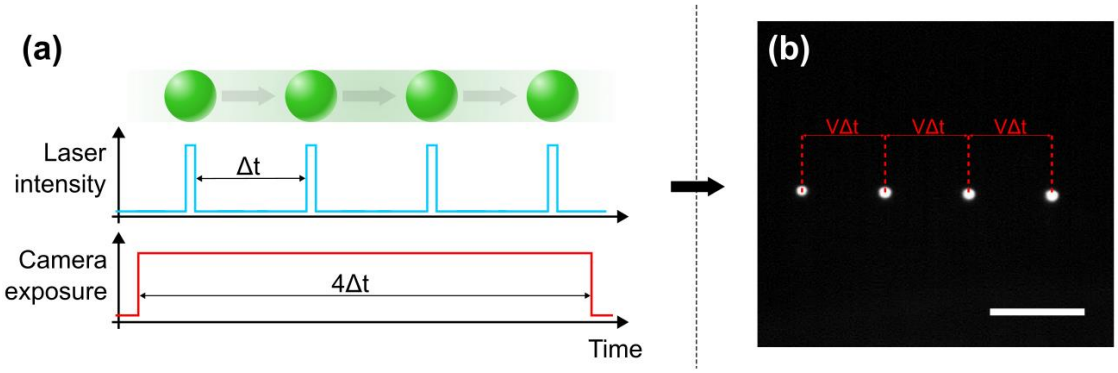

Figure 3.7 Strobing the laser enables easily computable speed measurement in a single image frame. (a) The same bead is seen 4 times on the same image as it goes through the channel while being periodically irradiated (b) Real data taken with this set up with annotations in red. The four bright disks are the same bead. Scalebar: 100µm

By localizing the disks positions and associating each series of disks with a single bead (as part of the data presents several beads on the same image), we can compute the average speed in the channel given the radial position of the object in the channel.

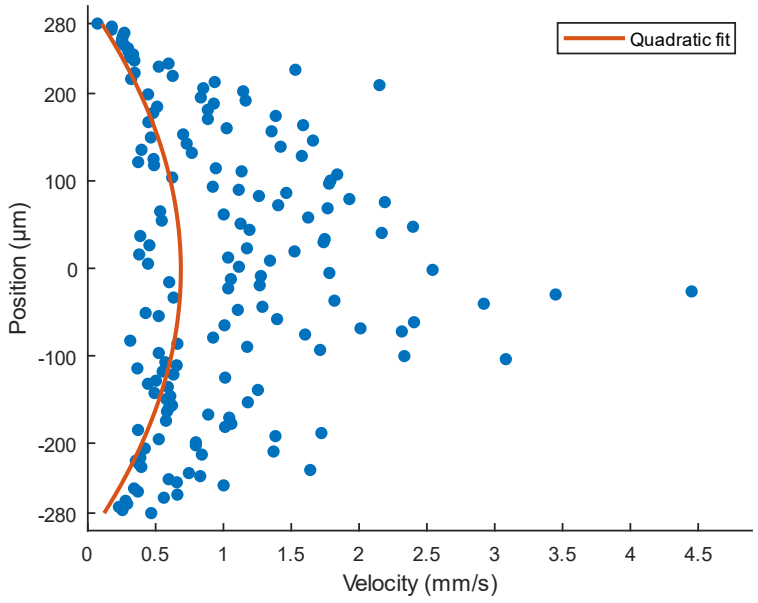

Figure 3.8 Velocity mapping shows high heterogeneity. Velocity is given in a.u.

It is important to note that the curve of the theoretical flow is not a simple quadratic since it is the integral over one axis of the flow profile in a square channel. It partially explains the heterogeneity of the scatter plot; because of the important depth of field of the set up, some beads were observed

as they were passing in a corner of the cross section while others were only close to an edge, hence having different velocities despite showing at the same place on the camera.

We will show in the next part that even a slight speed inhomogeneity completely disrupts the order of the sequences on macroscopic scales, and how it makes it practically impossible to solve the problem without changing the strategy.

3.5 Flow focusing

The first models we considered for this problem assumed that the order of the beads could change due to diffusion in the flow, and the algorithms showed an impressive robustness to this possibility. Indeed, we were expecting the properties of inertial flow focusing to homogenize the velocities of the beads well enough for just a fraction of them to overtake each other.

However, we showed with *Figure 3.8* that velocity ratios as high as 3 were to expect. In order to evaluate how much of a problem two beads overtaking each other is, we will show that in order to keep the problem solvable, an inhomogeneity in the speed distribution needs to be either negligible or precisely characterized.

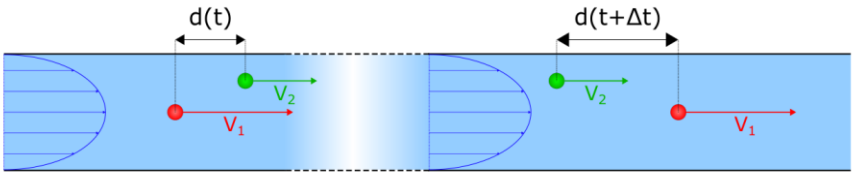

Figure 3.9 Inhomogeneous velocities leads to overtaking events. The red bead, which was behind in the first place, ends up being before the green bead after a time Δt.

Given two objects with constant speeds of respectively V_1 and V_2, separated by a distance d(t) at time t, we can predict their positions further down the channel. There are then two ways to tackle the problem:

- Measure the speeds V_1 and V_2 with enough accuracy, so that the order of the objects further down the channel can be estimated with precision.
- Act on the sparseness of the objects in the flow or the speed homogeneity to make overtaking events negligible.

Here we show that the two approaches obey the same requirements. If we write:

$$d(t + \Delta t) = d(t) + \Delta d \text{ and } V_1 = V_2 + \Delta V$$

Where d is the axial distance separating two consecutive objects in the channel.

The immediate result is:

$$\Delta d = \Delta V \Delta t \tag{3.1}$$

Δt is the time that it takes for the objects to reach the second measurement point:

$$\Delta t \sim \frac{D}{V} \tag{3.2}$$

with V the average speed of the objects within the flow and D the distance between the two measurement points.

Whether it is to estimate the distance between the two objects accurately enough or to limit overtaking, the condition on Δd is:

$$\Delta d < d \tag{3.3}$$

Then, by combining equations (3.1), (3.2) and (3.3), we can write equation (3.4):S

$$d > \frac{\Delta V}{V} D \tag{3.4}$$

For the following estimation, we consider D ~ 1m as the aim of the project is to track micro-scale objects on meter-scale distances. For 10µm beads 100µm apart on average, this translates to a ΔV/V ratio of 0.01%. Measuring the speeds with so much precision is not feasible for this project, and managing to get speeds as homogeneous as this is extremely challenging.

Another way to fulfill this condition is to increase the value of d, which reduces the throughput. Before establishing a feasible maximum value for d, the aim is to lower the ΔV/V ratio as much as possible.

This is precisely the purpose of flow focusing.

3.5.1 Acoustic flow focusing

Frequently used in modern flow cytometers, acoustic flow focusing relies on the interaction of particles with a pressure field created by the propagation of sound waves within the flowing medium. The force experienced by an object immersed in medium subject to an acoustic pressure field is given by equation (3.5) [77]:

$$F = -\left(\frac{\pi p_0^2 V_p \beta_m}{2\lambda}\right) \cdot \phi(\beta, \rho) \cdot \sin(2kx) \tag{3.5}$$

With p_0 the amplitude of the pressure wave, V_p the volume of the particle, β_m the compressibility of the medium and λ the wavelength. The sine term describes the position of the particle on the wave. $\phi(\beta, \rho)$ is the Acoustic Contrast Factor (ACF), and it is given by the equation (3.6):

$$\phi(\beta, \rho) = \frac{5\rho_p - 2\rho_m}{2\rho_p + \rho_m} - \frac{\beta_p}{\beta_m} \tag{3.6}$$

Here, ρ_p is the density of the particle, ρ_m the density of the medium, β_p is the compressibility of the particle, and β_m is the compressibility of the medium. On a standing wave, a positive acoustic factor implies that the particle drifts towards pressure nodes while a negative one implies that the particle drifts towards pressure antinodes.

As stated earlier, the medium was adapted to minimize buoyancy effects. Given that the compressibility of a mixture is well-approximated by the weighted sum of the compressibility of its components [78], we can estimate the ACF of the polystyrene beads immersed in a water-ethanol mixture, where the density of polystyrene beads was estimated to be 0.9895.

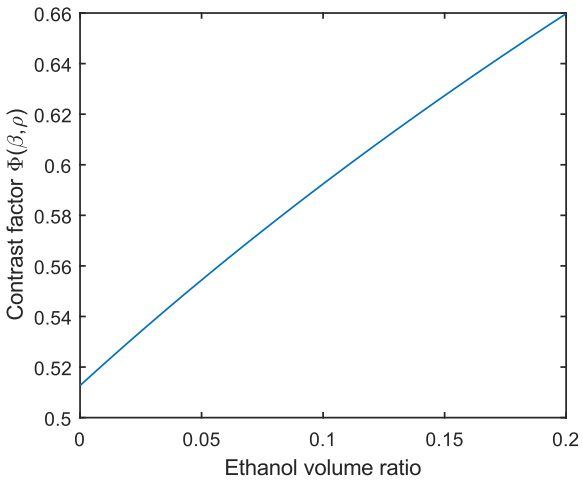

Figure 3.10 Calculated ACF (Equation (3.6)) of polystyrene beads in a water-ethanol mixture. Adding ethanol to water does not have an impactful effect on the bead/mixture acoustic properties.

The positive ACF indicates that the beads are pushed towards pressure nodes, and adding ethanol in the medium does not have a major influence on the beads capacity to be focused using acoustic waves.

3.5.1.1 Methodology

The experimental objective is then to generate and maintain a standing wave inside the channel to focus the particles within the channel, so that their velocity is more homogeneous. In order to get only one stream of particles, it is necessary to get a standing wave with only one pressure node within the channel. To achieve this, the channel width needs to be half the wavelength of the pressure wave.

The acoustic wave is generated using a piezoelectric element. A piezoelectric element has a resonant frequency at which the amplitude of the soundwave it generates peaks, hence producing the highest pressure and the highest force on the particles. Affordable piezoelectric elements in the MHz range are challenging to find; to fulfill the low-cost aim of this project, the choice fell on industrially available ceramic piezo elements used in ultrasonic atomizers.

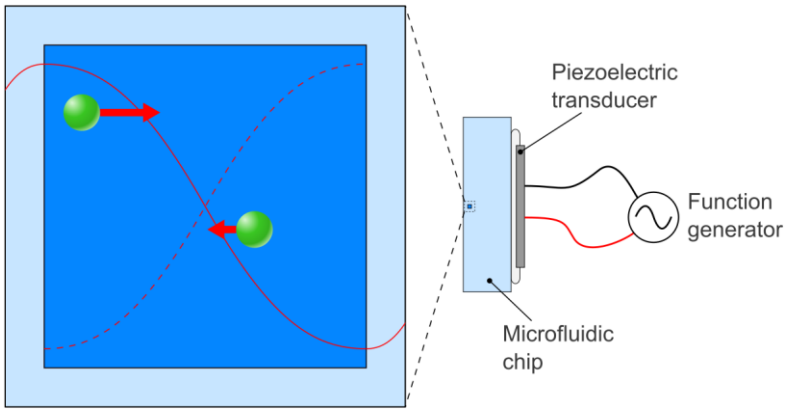

Figure 3.11 Acoustic focusing inside a microfluidic channel: The incident and reflected wave create a standing wave inside the channel

A first experiment was set to assess both the efficiency of the piezo transducer and the acoustic impedance of the microscope slide used. An estimation of the piezo transducers transfer function was established, using the setup described by Figure 3.12:

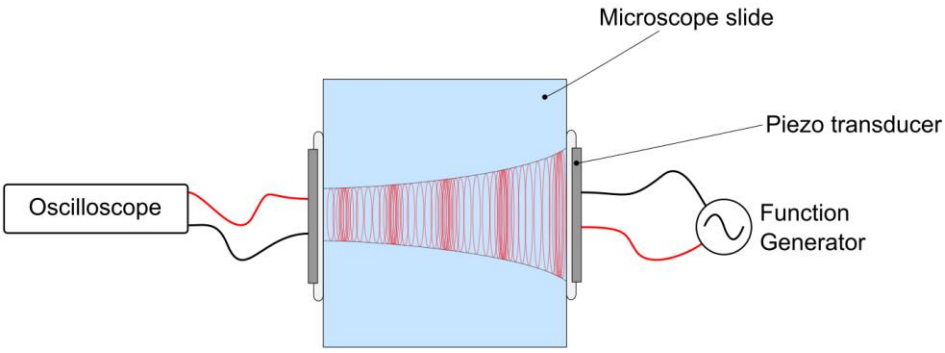

Figure 3.12 Diagram of the setup used to evaluate the piezo transducers transfer function and microscope slide's acoustic impedance. The microscope slide is 1.3mm thick.

The transfer function was estimated around the resonant frequency by sweeping through evenly spaced frequencies with the function generator and measuring the amplitude of the output on the oscilloscope:

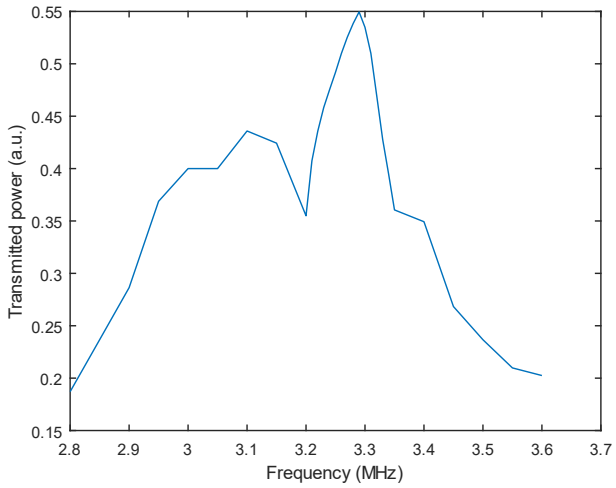

Figure 3.13 Estimation of the piezo elements transfer function around the theoretical resonance frequency: The curve is the square root of the measured voltages since a piezo is used both as the emitter and receptor, multiplying by the transfer function twice.

This estimation relies on the hypothesis that the transfer function of the piezo transducer is the same whether it is used as an actuator (emission) or a sensor (reception).

The propagation of the soundwave through the glass slide and interfaces between media (epoxy resin, glass, water and ethanol) is highly non-trivial, and predicting the positions of the nodes and antinodes demands a clear modeling of the components and their behavior in a pressure field [40]. The empirical nature of this project as well as other arguments (see part 3.4.2 Steadiness of the

flow along the channel) pushed the experiments towards observation of the phenomenon without prior modeling, using the setup described in Figure 3.14:

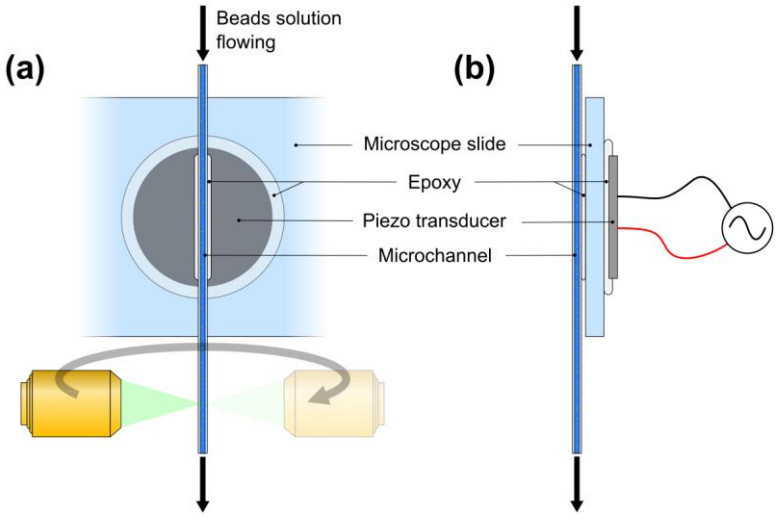

Figure 3.14 Diagram of the setup to induce and observe acoustic flow focusing: (a) Front view, beads are constantly flowed through the channel while AC voltage is applied to the piezo transducer. The piezo and channel part can be rotated to be imaged at different angles not to miss a planar focusing (b) Side view

The aim of this setup is to allow for observation of the flow from different angles since the geometry of the standing wave that we aim to generate is mostly unknown. Focusing along a plane that is not orthogonal to the focal plane could be unnoticed.

3.5.1.2 Results

While observing live images of the fluorescent bead stream from the camera, we scanned a range of frequencies from 2 to 4 MHz with the function generator. The operation was repeated at several observation angles, with no change in the bead flow observed.

Several piezo transducers were tested with different systems, and a different adhesive was used to bond the transducer and microchannel to the microscope slide. In all cases, no change in bead flow was observed.

The inconclusive results of this experiment may be attributed to poor acoustic wave propagation in the system, due to its geometry or the nature of the materials used. It is also possible that the piezo transducers used, which are very inexpensive and whose primary use is not the one for which they were used here, do not provide the necessary power to move the beads in the flow.

3.5.2 Flow stability in the channel

Before diving too deep in acoustic flow focusing or any kind of flow focusing method, it is important to evaluate how long the focusing effect can last inside a microfluidic channel. There is no use in focusing the particles only for a short distance, as the speeds need to stay homogeneous over the whole length of the tube.

3.5.2.1 Methodology

The following experiment was setup to evaluate how constant the individual beads velocity stayed as they flow along the tube, and how easy it would be to match beads knowing their velocity.

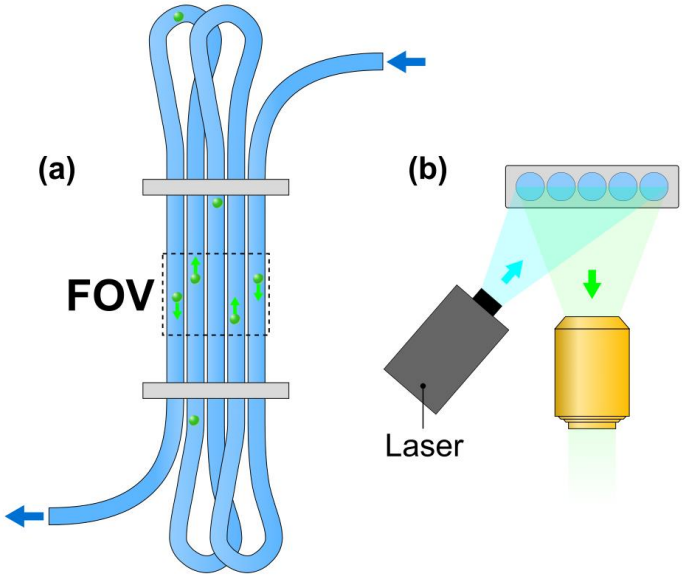

Figure 3.15 Diagram of the experimental setup used to evaluate the beads velocity evolution along time: (a) (Front view) The tube is twisted so that several sections appear on camera (b) (Top view) All tube sections are illuminated with a horizontal-lign-shaped laser beam

By observing several passes of the beads at different points in the pipe, and measuring their speed, we can attempt to match the objects detected. To do this, we use a solution of fluorescent beads sufficiently diluted to make detections rare and thus facilitate matching. As in previous experiments, the beads are diluted in a mixture of water and ethanol to equalize their density with that of the liquid.

3.5.2.2 Results

Measuring velocity at two different points enables us to match the beads despite a change in velocity along the flow, on the assumption that the change in velocity is sudden and always takes place at the same point (e.g., in a bend, because of an impurity in the tube that disrupts the flow). To do this, we use the reasoning shown in Figure 3.16:

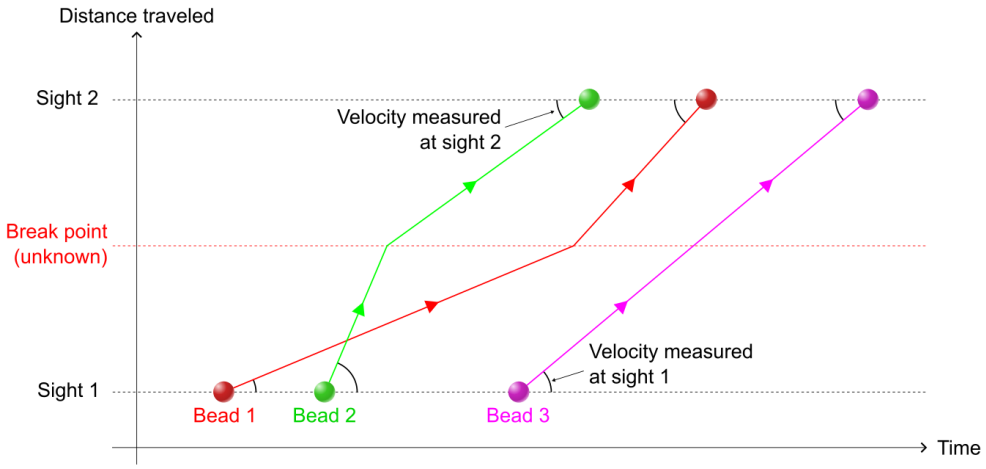

Figure 3.16 Seeing beads twice and measuring their speed allows to match them despite a single speed change. The breakpoint is the place where the intersection between the upper and lower slopes happens, and it is a priori unknown. This is based on the hypothesis that the speed of the objects changes at the same position in the tube.

The beads seen for the first time maintain a roughly constant speed until they reach the breakpoint, where their speed changes to that measured on the second pass through the FOV. In the diagram, the height of the breakpoint is a priori unknown. The strategy then consists in (1) placing the beads at the times and places where they were seen, (2) plotting the slopes given by their velocities, (3) establishing the points of intersection between the slopes, (4) finding the most consistent breakpoint location. If the break point model is correct, we expect to find a predominance of slope intersections at the break point on the graph. To do this, we separate the population of slope intersection points into clusters and see if one of the clusters (in theory, the one at the break point) dominates.

This method also proved ineffective in matching different views of a bead with each other, indicating that either the speed of the beads changed significantly and constantly as they advanced through the tube, or that many beads passed through the FOV without being measured. Imaging at low magnification (to fit all five tubes into the FOV) and the deflection of light rays by the

cylindrical walls of the tubes made acquisition conditions too difficult to refute the second explanation of the missing beads.

Because of the complexity of imaging and matching beads even in configurations thought to be simple, and the impossibility to try the algorithms on real data, a solution was needed to move towards the proof of concept. The idea to encapsulate beads and cells inside arbitrarily large droplets before flowing them would make the overtaking events virtually impossible, thus nullifying all considerations about sequences becoming too different from one point to another.

3.6 Microfluidics and droplet generation

For several experiments, we have needed specific geometries for microfluidic chips. To thwart the time and cost constraints brought by buying microfluidic chips from outside companies, a part of this project has been oriented towards creating microfluidic chips using unusual methods: 3D printing and laser cutting.

3.6.1 3D printing microfluidic devices

3D printing is a technology that has undergone a meteoric rise in recent years, and now finds itself equipping most laboratories at low cost. Additive printing by successive polymerization of very thin slices of resin makes it possible, in principle, to manufacture any monolithic structure within the limits of resolution. This overcomes the 2D limitation of most conventional methods, such as soft lithography. In addition to the ability to create 3D pipelines, SLA also enables any 3D-modelled chip to be produced in parallel, at low cost and satisfactory speed. In practice, however, several phenomena limit the capabilities of this technology, at least with a commercial printer.

3.6.1.1 Methodology

The laboratory is equipped with a SLA 3D printer, the Phrozen Sonic Mini 8K. It has a resolution of 21µm in the printing plane, and z-axis resolution down to 10µm. These resolutions, although not as detailed as those possible with soft lithography which reaches 10nm [79], make it theoretically possible to print microfluidic devices with dimensions in excess of 100µm.

In order to be able to observe the inside of the printed devices, we used a transparent resin. Each print is parameterized by the duration of exposure to UV light, the z-axis resolution and, above all,

the orientation of the parts to be printed. *Figure 3.17* shows a device designed to experiment with sheath fluid flow focusing. Several devices were printed, starting with 10:1 scale models.

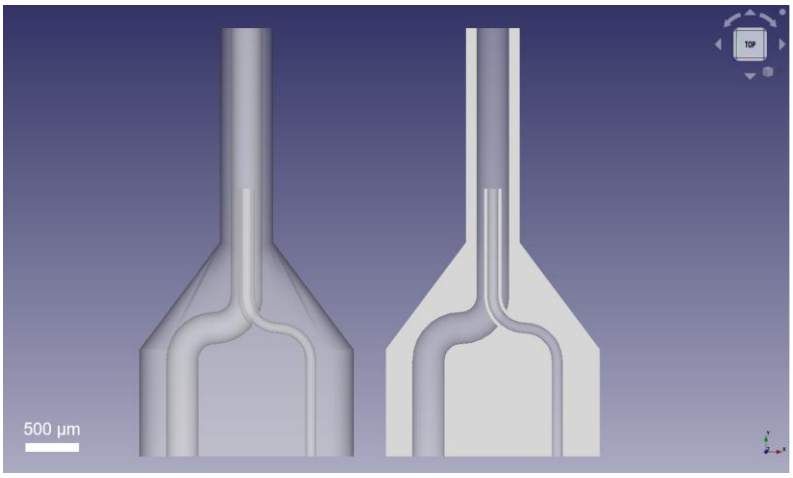

Figure 3.17 3D model of a sheath fluid device: The right part is a half cut printed as is to be bonded with the matching other half.

3.6.1.2 Results and limitations

Full-scale impressions (around 100µm) of channels are not possible with the techniques deployed in these experiments. All channels smaller than 1mm in diameter and longer than 1cm are plugged with solidified resin, no matter the parameters. One technique deployed to increase resolution is to print the channel in two parts, by making an axial cut (illustrated by the component on the right of Figure 3.17). The two halves are then glued together by hand. This technique can be useful for rigid devices with dimensions at least in the millimeter range, as alignment is in practice complex to achieve during the gluing part. Other techniques are possible, such as printing the channel negative from a wax-like resin that can then be cast. This technique may be of interest for microfluidic devices where printing in three dimensions is necessary; for flat devices, laser cutting is preferable.

3.6.2 Laser cutting microfluidic devices

3.6.2.1 Methodology

The manufacturing principle consists in stacking three different layers, as shown in *Figure 3.18*:

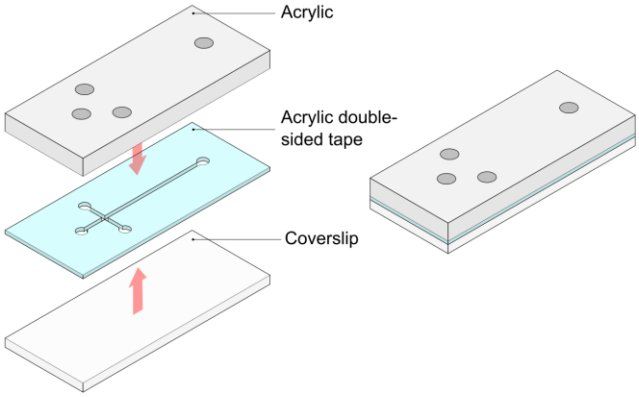

Figure 3.18 Diagram of the laser-cut chip assembly: Both the top and middle part are hollowed with a laser cutter. The double-sided tape is 30µm thick.

Using a laser cutter, the microfluidic circuit is carved in 30µm thick acrylic adhesive double-sided transfer tape (intermediate layer). Holes are drilled in a layer of 1/4" acrylic slab used for rigidity and transparency, and to connect the circuit to the pumps. The microfluidic channel is sealed on the other side by a coverslip to enable close-up imaging with an objective.

Cutting was carried out at Polyfab using a Trotec Speedy 400 Flexx cutter, which employs a CO_2 laser. To maximize ablation precision, cuts were made with the shortest focal length lens available, i.e., two inches.

To optimize cutting precision, it is possible to modify the lens used to focus the cutting laser, as well as to modulate laser power, the speed at which it is moved over the material to be cut, and the number of passes. Several benchmarking chips were carried out to establish the best parameters.

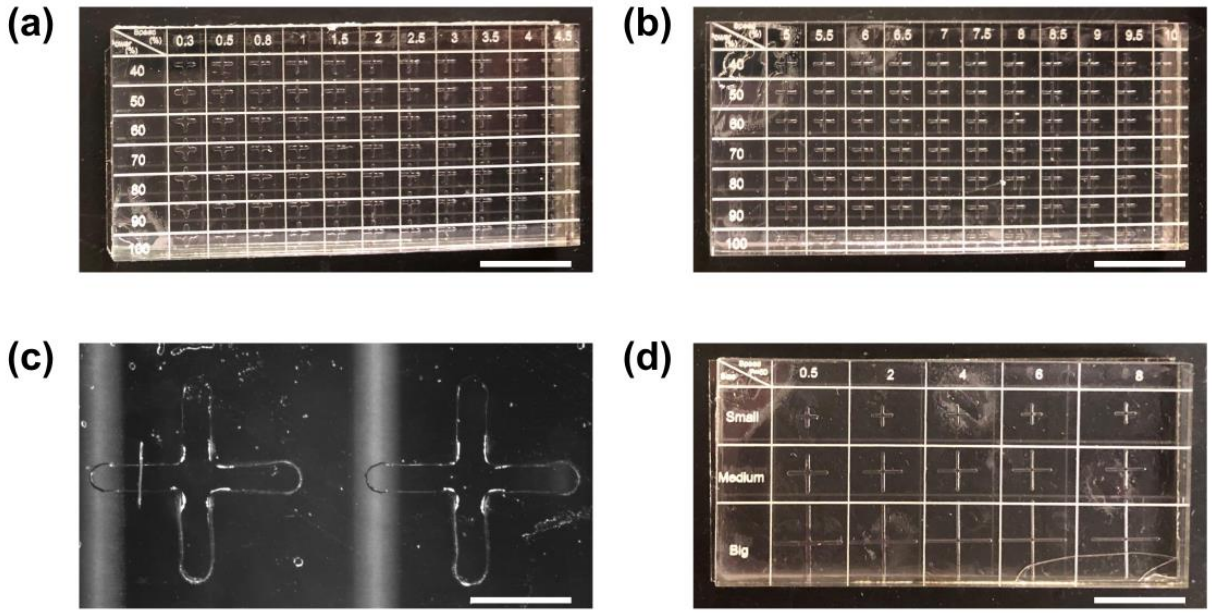

Figure 3.19 Benchmarking chips to evaluate the right parameters for the laser cutter: (a,b) Every column is associated with a laser lateral speed (% of maximum speed), every row with a laser power (% of maximum power), scalebar: 1cm (c) Detail of two crosses used as a benchmark, scalebar: 1mm (d) Every line is associated with a laser lateral speed (% of maximum speed), every row with a cross size because the laser cannot reach full speed when cutting small structures, scalebar: 1cm

According to the results given by the benchmarking, a power of 60% and a speed of 4% were used to cut the following chips.

To interface the chips with the pumps, flat-tipped needles are inserted into holes in the acrylic. The chip-needle interface is then sealed with epoxy, and the tubes are connected to the needles.

To characterize the cut tracks, we used an optical microscope and several magnifications to observe the different scales. Samples are back illuminated under white light.

3.6.2.2 Results and limitations

Several models have been produced, ranging from simple self-pumping channels using capillary forces to droplet generation devices. The chips produced are perfectly sealed and can withstand the pressures imposed by the pumps.

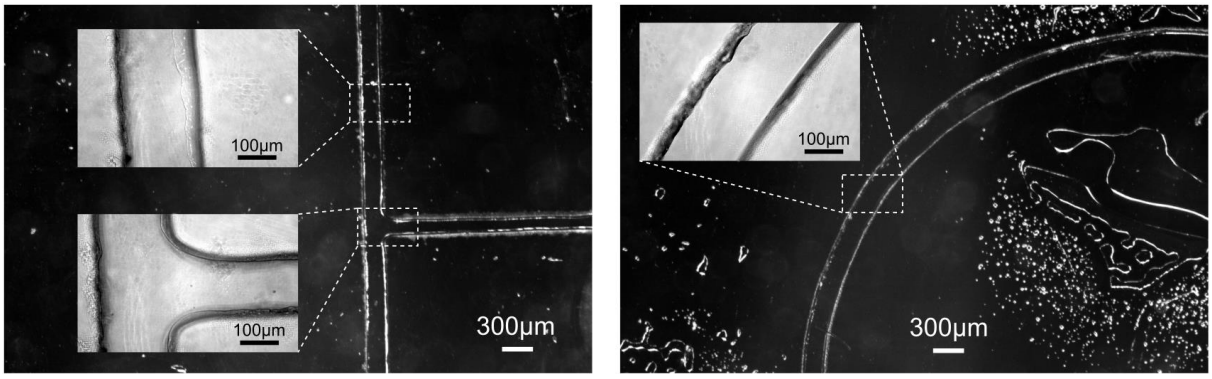

Figure 3.20 Laser cut microfluidic channels.

Laser cutting enables to produce highly customizable microfluidic circuits in a reasonable time. Excluding design, each chip takes around 10 minutes to build. The only size limitation is that of the coverslip, which is the only element whose contours cannot be cut.

Three limitations have been identified. Firstly, the hollowed-out tracks have irregular walls, which disrupt the flow in the channel. Secondly, this method does not allow all geometries to be cut; the channels must not form a loop, in which case the double-sided tape would be split into several parts, making assembly practically impossible. Finally, channel width is difficult to control. The channels carved in this experiment were performed by one single laser pass, and therefore to the minimum achievable width. Carving slightly larger channels is challenging as the resolution is of the order of the channel width.

3.6.3 Droplet generation

The main problem of this project is to prevent objects from overtaking each other during transport. Encapsulating them in droplets increases their effective size in the duct, with the aim of homogenizing velocities and making the droplets screen each other, thus preventing overtaking.

The challenges of this strategy lie in generating droplets of controlled size, and above all in ensuring that they are stable enough not to merge with their neighbors during transport.

3.6.3.1 Methodology

Some of the chips used were purchased from ChipShop, while others were manufactured here using a laser cutter. The aqueous phase is made from pure water, while two oil phases were tested:

paraffin and coconut oil. Surface tension is reduced by Tween-80, a surfactant soluble in aqueous phase.

To assess the proportion of surfactant needed to stabilize a water-in-oil emulsion, we first studied the stability of heterogeneous emulsions produced using an ultrasonic bath. After making the emulsions with different surfactant concentrations, they were left to stand for one hour before being observed under a white-light, back illuminated microscope. The concentration of Tween-80 that was giving the smallest droplets was selected (10% v/v).

The droplet generators are then connected to pumps, one pressurizing the oil phase and the other the water phase. The droplet nucleation site is then observed under the microscope, and the droplets are transported to a reservoir for observation after generation (Figure 3.21).

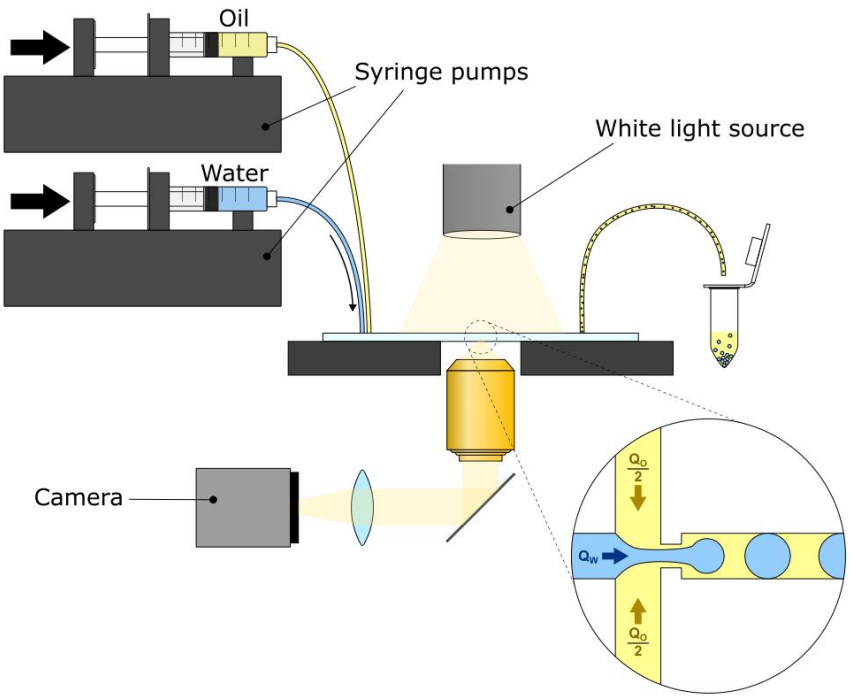

Figure 3.21 Diagram of the set up used to monitor droplet generation.

Water and oil phase flow rates are controlled independently.

3.6.3.2 Results and limitations

We were able to create droplets, and we briefly studied the influence of the ratio $\frac{Q_0}{Q_w}$ on droplet generation in this configuration.

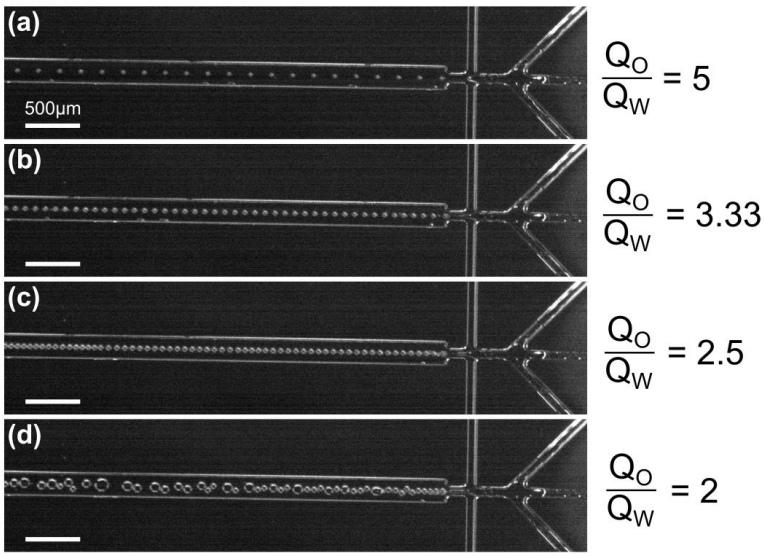

Figure 3.22 Influence of the flow ratios on droplets: the droplets get bigger and more frequent, until they start to merge together

The flow ratio influences both the size of the droplets and the frequency at which they are synthesized.

Panel (d) reveals the main limitation of the experiment: droplets fuse together as soon as they come into contact. The fusion of neighboring droplets continues until only large droplets remain in the tube.

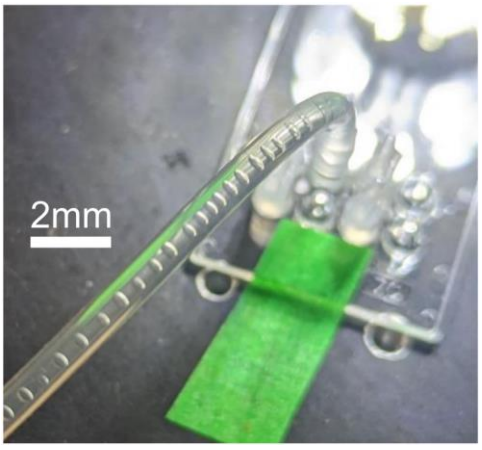

Figure 3.23 Droplets coalesce at the chip/tube interface to form macroscopic drops in the tube.

This limitation makes it impossible to use the system as it is. In a next step, the droplets should be made stable and slightly larger to be sure that they are big enough to solve the problem they were generated for: not overtaking by screening each other in the channel.

The choice of chemical components is central to process improvement. Experiments and literature indicate that Tween-80 is not the best choice of surfactant for water-in-oil emulsions using a microfluidic droplet generator. Similarly, other oils can be used to assess their effect on droplets. However, not all oils are compatible with microfluidic chips; coconut oil, although presenting ideal characteristics for droplet generation [80], embrittles all acquired chips, which then explode under pump pressure. Paraffin weakens Topas chips, which also break under pressure.

CHAPTER 4 CONCLUSION

In this work, we have proposed the development of a new strategy for a multimodal device in flow. In simulation, we can see that the approach is feasible so long as a key condition can be met: namely, there is not a significant amount of mixing in the device. In this project, which was the first microfluidics project carried out in the Weiss Lab, we have set up and tested several potential solutions to do so using a variety of off-the-shelf parts and custom microfluidic devices.

Specifically, we were able to provide a solution to several of the following objectives set out earlier:

Our work was the first of its kind to be carried out at the WeissLab. Although this project did not result in the assembly of a satisfactory solution to the initial problem, it did enable us to evaluate the way forward for further work.

Except for the bolded lines in the list, we were able to provide a solution to several of the objectives set out earlier:

(1) Moving microscopic samples
    a. Create a system of tubes and channels to move samples and image them in the flow.
    b. Assemble a system of servo-controlled pumps to control the flow and movement of objects.
(2) Detect and record sequences
    a. Set up a microscope to illuminate the beads and measure their fluorescence.
(3) Match different measurements of identical objects
    a. Establish an algorithm for aligning sequences of objects of any length.
    b. Evaluate the algorithm's capabilities with degraded sequences.

And leave the remaining objectives to be accomplished in future work:

(1) Keep the order of sequences as stable as possible when moving between measurements.

(2) Record and process the light signals detected at high throughput.

Even though observing some of the objects is easy, observing every object is remarkably difficult. The imaging conditions imposed by this project make data collection laborious, with many objects having multiple reflections appearing double or triple on the screen, and others seeing their light

deflected by a refracting wall appearing either not at all or very diminished. Imaging objects flowing inside transparent channels brings a great deal of uncertainty as to what is actually being observed and makes imaging conditions more difficult. These conditions impact on the system's ability to establish sequences, which form the basis of the tracking strategy. This means improving the imaging strategy or increasing the visibility of objects to be imaged somehow; using larger, brighter fluorescent beads.

On the other hand, inertial flow focusing has proved far less predominant than expected in alignment simulations. While it is widely demonstrated and used in standard-sized devices, it now seems certain that increasing the length of the problem and going beyond precisely designed microfluidic chips completely hinders the capacity of inertial flow focusing to homogenize the speeds within a duct. Looking forward, it's clear there are two main solutions: focusing or preventing mixing by using large objects or objects encapsulated in droplets.

It has been made clear in section 3.5 that solving the problem through flow focusing alone is particularly challenging. Flow focusing, using the material that we have been using, is not a reliable solution for large scales. However, the acoustic flow focusing strategy can be treated with more attention and budget than it has been in this work; microfabricated piezoelectric transducers organized regularly along the transport tube seem to be able to provide a satisfactory solution to the velocity homogeneity problem. Nonetheless, modelling the propagation of acoustic waves in the system requires considerable prior simulation work, and the technologies for manufacturing such transducers were not yet available in the lab. A system capable of operating based on flow focusing alone would certainly still work with droplets, making this strategy a more flexible and comprehensive solution than relying necessarily on droplets.

In section 3.5 we showed that maintaining the sequence order in free-flowing objects is particularly challenging. Looking forward, the natural next step is to achieve sequence alignment by encapsulating beads inside droplets. This is equivalent to simplifying the problem by an order of magnitude as the droplets could be treated as massive beads, hence nullifying the concerns of objects overtaking each other as they are transported from one place to another. In this regard, we approached the problem in several different ways: 3D printing full devices, layered laser-cutting materials and commercially purchasing chips. The former would seemingly be advantageous for flexibility, but limitations in print resolution and channel blocking at these scales posed a major

problem. Layered laser-cut materials, although showing promising alternatives for creating custom devices, lack the precision needed to create emulsions of great regularity. It remains a viable solution for the production of other devices requiring less precision. Finally, the purchase of commercial products limits customization possibilities, and poses compatibility problems with certain materials that cannot be circumvented. A possible alternative for the future creation of custom devices is soft lithography and the use of PDMS, which would enable the creation of more controlled conditions for testing hypotheses on a small scale.

Although one of the main features of the envisaged solution is its low cost, achieving a proof-of-concept with inexpensive hardware is an additional challenge. In hindsight, it seems more sensible to build an expensive functional system before replacing its components one by one, trying to maintain performance as the price drops. The measuring devices were assembled by us, and the setup used cost around $3,000 (including $600 for the camera, which will be removed, and $2,000 for the pumps); it was however not performing well enough.

In conclusion, this work outlines a path for future research, while the ultimate objective of building a functional multimodal device has not yet been achieved, we now better understand the main obstacles to overcome. Challenges with imaging and inertial flow focusing underscore opportunities for advancement. The transition to droplet-based alignment appears promising, alongside exploration of acoustic flow focusing. Fabrication methods like soft lithography hold potential. Striking a balance between cost and functionality remains a hurdle. One way to solve this problem is through a gradual hardware development approach, where more established and costly components can be replaced one by one with lower cost ones.

REFERENCES

[1] B. C. Buchanan and J.-Y. Yoon, “Microscopic Imaging Methods for Organ-on-a-Chip Platforms,” *Micromachines (Basel)*, vol. 13, no. 2, p. 328, Feb. 2022, doi: 10.3390/mi13020328.

[2] J. Park *et al.*, “Quantification of structural heterogeneity in H&E stained clear cell renal cell carcinoma using refractive index tomography,” *Biomed Opt Express*, vol. 14, no. 3, pp. 1071–1081, Feb. 2023, doi: 10.1364/BOE.484092.

[3] J. A. Ramos-Vara, “Technical Aspects of Immunohistochemistry,” *Vet Pathol*, vol. 42, no. 4, pp. 405–426, Jul. 2005, doi: 10.1354/vp.42-4-405.

[4] L. E. Morrison *et al.*, “Brightfield multiplex immunohistochemistry with multispectral imaging,” *Lab Invest*, vol. 100, no. 8, Art. no. 8, Aug. 2020, doi: 10.1038/s41374-020-0429-0.

[5] J. D. L. Ong, E. G. T. Abigan, L. G. Cajucom, P. A. R. Abu, and Ma. R. J. E. Estuar, “Ensemble Convolutional Neural Networks for the Detection of Microscopic Fusarium Oxysporum,” in *Advances in Visual Computing*, G. Bebis, Z. Yin, E. Kim, J. Bender, K. Subr, B. C. Kwon, J. Zhao, D. Kalkofen, and G. Baciu, Eds., in Lecture Notes in Computer Science, vol. 12509. Cham: Springer International Publishing, 2020, pp. 321–332. doi: 10.1007/978-3-030-64556-4_25.

[6] Y.-X. Huang, C.-L. He, P. Wang, Y.-T. Pan, W.-W. Tuo, and C.-C. Yao, “Versatile on-stage microfluidic system for long term cell culture, micromanipulation and time lapse assays,” *Biosensors and Bioelectronics*, vol. 101, pp. 66–74, Mar. 2018, doi: 10.1016/j.bios.2017.09.041.

[7] F. Rudek, T. Puder, C. Taudt, and P. Hartmann, “Multispectral imaging system for the structural analysis of highly transparent technical surfaces,” 2019, Accessed: Aug. 15, 2023. [Online]. Available: https://publica.fraunhofer.de/handle/publica/404861

[8] K. Yoshimura, null Patmawati, M. Maeda, N. Kamiya, and T. Zako, “Protein-Functionalized Gold Nanoparticles for Antibody Detection Using the Darkfield Microscopic Observation of Nanoparticle Aggregation,” *Anal Sci*, vol. 37, no. 3, pp. 507–511, Mar. 2021, doi: 10.2116/analsci.20SCP12.

[9] T. E. Moustafa, E. R. Polanco, R. L. Belote, R. L. Judson-Torres, and T. A. Zangle, "Fabrication and validation of an LED array microscope for multimodal, quantitative imaging," *HardwareX*, vol. 13, p. e00399, Mar. 2023, doi: 10.1016/j.ohx.2023.e00399.

[10] M. Qi, C. Darviot, S. Patskovsky, and M. Meunier, "Cost-effective side-illumination darkfield nanoplasmonic marker microscopy," *Analyst*, vol. 144, no. 4, pp. 1303–1308, Feb. 2019, doi: 10.1039/C8AN01891J.

[11] F. Zernike, "Phase contrast, a new method for the microscopic observation of transparent objects," *Physica*, vol. 9, no. 7, pp. 686–698, Jul. 1942, doi: 10.1016/S0031-8914(42)80035-X.

[12] T. H. Nguyen *et al.*, "Halo-free Phase Contrast Microscopy," *Sci Rep*, vol. 7, no. 1, Art. no. 1, Mar. 2017, doi: 10.1038/srep44034.

[13] T. Lambert, "EGFP at FPbase," *FPbase*. https://www.fpbase.org/protein/egfp/ (accessed Aug. 12, 2023).

[14] Y. Wang, H. Chen, C. Li, and P. Wu, "Octachloro-fluorescein: Synthesis and photosensitizer performance evaluation," *Dyes and Pigments*, vol. 170, p. 107635, Nov. 2019, doi: 10.1016/j.dyepig.2019.107635.

[15] P. Tandale *et al.*, "Fluorescent quantum dots: An insight on synthesis and potential biological application as drug carrier in cancer," *Biochemistry and Biophysics Reports*, vol. 26, p. 100962, Jul. 2021, doi: 10.1016/j.bbrep.2021.100962.

[16] A. Chandra, S. Prasad, G. Gigli, and L. L. del Mercato, "Chapter 6 - Fluorescent nanoparticles for sensing," in *Frontiers of Nanoscience*, W. J. Parak and N. Feliu, Eds., in Colloids for Nanobiotechnology, vol. 16. Elsevier, 2020, pp. 117–149. doi: 10.1016/B978-0-08-102828-5.00006-1.

[17] K. Chen, W. Li, and K. Xu, "Super-multiplexing excitation spectral microscopy with multiple fluorescence bands," *Biomed Opt Express*, vol. 13, no. 11, pp. 6048–6060, Oct. 2022, doi: 10.1364/BOE.473241.

[18] J. Ghanam *et al.*, "Single Molecule Localization Microscopy for Studying Small Extracellular Vesicles," *Small*, vol. 19, no. 12, p. 2205030, 2023, doi: 10.1002/smll.202205030.

[19] J. Son, B. Mandracchia, A. D. Silva Trenkle, G. A. Kwong, and S. Jia, “Portable light-sheet optofluidic microscopy for 3D fluorescence imaging flow cytometry,” *Lab Chip*, vol. 23, no. 4, pp. 624–630, 2023, doi: 10.1039/D2LC01024K.

[20] O. Reynolds, “On the Dynamical Theory of Incompressible Viscous Fluids and the Determination of the Criterion,” *Philosophical Transactions of the Royal Society of London. A*, vol. 18, pp. 123–164, 1895.

[21] Z. Rek and B. Šarler, “The method of fundamental solutions for the Stokes flow with the subdomain technique,” *Engineering Analysis with Boundary Elements*, vol. 128, pp. 80–89, Jul. 2021, doi: 10.1016/j.enganabound.2021.03.020.

[22] P. J. A. Kenis, R. F. Ismagilov, and G. M. Whitesides, “Microfabrication Inside Capillaries Using Multiphase Laminar Flow Patterning,” *Science*, vol. 285, no. 5424, pp. 83–85, Jul. 1999, doi: 10.1126/science.285.5424.83.

[23] L. Cai, J. Marthelot, and P.-T. Brun, “An unbounded approach to microfluidics using the Rayleigh–Plateau instability of viscous threads directly drawn in a bath,” *Proceedings of the National Academy of Sciences*, vol. 116, no. 46, pp. 22966–22971, Nov. 2019, doi: 10.1073/pnas.1914270116.

[24] Z. Chen, S. Kheiri, E. W. K. Young, and E. Kumacheva, “Trends in Droplet Microfluidics: From Droplet Generation to Biomedical Applications,” *Langmuir*, vol. 38, no. 20, pp. 6233–6248, May 2022, doi: 10.1021/acs.langmuir.2c00491.

[25] T. M. Squires and S. R. Quake, “Microfluidics: Fluid physics at the nanoliter scale,” *Rev. Mod. Phys.*, vol. 77, no. 3, pp. 977–1026, Oct. 2005, doi: 10.1103/RevModPhys.77.977.

[26] N. M. Kovalchuk and M. J. H. Simmons, “Review of the role of surfactant dynamics in drop microfluidics,” *Advances in Colloid and Interface Science*, vol. 312, p. 102844, Feb. 2023, doi: 10.1016/j.cis.2023.102844.

[27] H. A. Pohl, “The Motion and Precipitation of Suspensoids in Divergent Electric Fields,” *Journal of Applied Physics*, vol. 22, no. 7, pp. 869–871, Apr. 2004, doi: 10.1063/1.1700065.

[28] K. Khoshmanesh, S. Nahavandi, S. Baratchi, A. Mitchell, and K. Kalantar-zadeh, “Dielectrophoretic platforms for bio-microfluidic systems,” *Biosensors and Bioelectronics*, vol. 26, no. 5, pp. 1800–1814, Jan. 2011, doi: 10.1016/j.bios.2010.09.022.

[29] L. Junwang, S. Penghui, Y. Duli, and X. Xiaoxing, “Dielectrophoresis-Based Blood Plasma Extraction using Two-Layer Conducting-PDMS Microelecrodes,” in *2022 IEEE 17th International Conference on Nano/Micro Engineered and Molecular Systems (NEMS)*, Apr. 2022, pp. 162–166. doi: 10.1109/NEMS54180.2022.9791192.

[30] H. N. Thu, Y.-V. T. Thi, H. B. Thu, H. T. T. Thuy, T. T. Bui, and L. D. Quang, “A Combination of Dielectrophoresis and Magnetophoresis Microfluidic Chip for Cancer Cells Separation,” in *2022 2nd International Conference on Intelligent Cybernetics Technology & Applications (ICICyTA)*, Dec. 2022, pp. 128–133. doi: 10.1109/ICICyTA57421.2022.10038082.

[31] H. Zhang, H. Chang, and P. Neuzil, “DEP-on-a-Chip: Dielectrophoresis Applied to Microfluidic Platforms,” *Micromachines (Basel)*, vol. 10, no. 6, p. 423, Jun. 2019, doi: 10.3390/mi10060423.

[32] G. Sitbon, R. W. Chantrell, and W. Schwarzacher, “The effects of anisotropy on solvent-suspended ‘superparamagnetic’ nanoparticles: Magnetization step on melting,” *Journal of Magnetism and Magnetic Materials*, vol. 503, p. 166486, Jun. 2020, doi: 10.1016/j.jmmm.2020.166486.

[33] A. Bakhshi, E. H. Nasab, V. Ghafouri, M. Rahmanian, and M. Badieirostami, “Design and Demonstration of a Novel Microfluidic Channel for Trapping Circulating Tumor Cells with Magnetophoresis,” in *2021 29th Iranian Conference on Electrical Engineering (ICEE)*, May 2021, pp. 74–77. doi: 10.1109/ICEE52715.2021.9544197.

[34] T. A. Burinaru *et al.*, “Antibody functionalized magnetic nanoparticles for circulating tumor cells detection and capture using magnetophoresis,” *IOP Conf. Ser.: Mater. Sci. Eng.*, vol. 485, p. 012005, Mar. 2019, doi: 10.1088/1757-899X/485/1/012005.

[35] A. Ashkin, J. M. Dziedzic, J. E. Bjorkholm, and S. Chu, “Observation of a single-beam gradient force optical trap for dielectric particles,” *Opt. Lett., OL*, vol. 11, no. 5, pp. 288–290, May 1986, doi: 10.1364/OL.11.000288.

[36] S. Luro, L. Potvin-Trottier, B. Okumus, and J. Paulsson, “Isolating live cells after high-throughput, long-term, time-lapse microscopy,” *Nat Methods*, vol. 17, no. 1, pp. 93–100, Jan. 2020, doi: 10.1038/s41592-019-0620-7.

[37] Z. Yao, C. C. Kwan, and A. W. Poon, “An optofluidic ‘tweeze-and-drag’ cell stretcher in a microfluidic channel,” *Lab Chip*, vol. 20, no. 3, pp. 601–613, Feb. 2020, doi: 10.1039/C9LC01026B.

[38] M. E. Piyasena *et al.*, “Multinode acoustic focusing for parallel flow cytometry,” *Anal Chem*, vol. 84, no. 4, pp. 1831–1839, Feb. 2012, doi: 10.1021/ac200963n.

[39] M. Baudoin *et al.*, “Spatially selective manipulation of cells with single-beam acoustical tweezers,” *Nat Commun*, vol. 11, no. 1, Art. no. 1, Aug. 2020, doi: 10.1038/s41467-020-18000-y.

[40] Z. Li, P. Li, J. Xu, W. Shao, C. Yang, and Y. Cui, “Hydrodynamic flow cytometer performance enhancement by two-dimensional acoustic focusing,” *Biomedical Microdevices*, vol. 22, Mar. 2020, doi: 10.1007/s10544-020-00481-9.

[41] Y. M. Patel, S. Jain, A. K. Singh, K. Khare, S. Ahlawat, and S. S. Bahga, “An inexpensive microfluidic device for three-dimensional hydrodynamic focusing in imaging flow cytometry,” *Biomicrofluidics*, vol. 14, no. 6, p. 064110, Dec. 2020, doi: 10.1063/5.0033291.

[42] A. Abdulla, W. Liu, A. Gholamipour-Shirazi, J. Sun, and X. Ding, “High-Throughput Isolation of Circulating Tumor Cells Using Cascaded Inertial Focusing Microfluidic Channel,” *Anal Chem*, vol. 90, no. 7, pp. 4397–4405, Apr. 2018, doi: 10.1021/acs.analchem.7b04210.

[43] B.-W. Li *et al.*, “Enhanced Separation Efficiency and Purity of Circulating Tumor Cells Based on the Combined Effects of Double Sheath Fluids and Inertial Focusing,” *Front Bioeng Biotechnol*, vol. 9, p. 750444, Oct. 2021, doi: 10.3389/fbioe.2021.750444.

[44] J. Lu *et al.*, “High-Throughput Cell Trapping in the Dentate Spiral Microfluidic Channel,” *Micromachines (Basel)*, vol. 12, no. 3, p. 288, Mar. 2021, doi: 10.3390/mi12030288.

[45] J. M. Nikoloff, M. A. Saucedo-Espinosa, A. Kling, and P. S. Dittrich, “Identifying extracellular vesicle populations from single cells,” *Proceedings of the National Academy of Sciences*, vol. 118, no. 38, p. e2106630118, Sep. 2021, doi: 10.1073/pnas.2106630118.

[46] T. Weisse and V. Bergkemper, “Rapid detection and quantification of the potentially toxic cyanobacterium Planktothrix rubescens by in-vivo fluorometry and flow cytometry,” *Water Research*, vol. 138, pp. 234–240, Jul. 2018, doi: 10.1016/j.watres.2018.03.052.

[47] “imec magazine October 2017 - Image sensor combining the best of different worlds.” https://www.imec-int.com/en/imec-magazine/imec-magazine-october-2017/image-sensor-combining-the-best-of-different-worlds (accessed Aug. 07, 2023).

[48] L. Yu, K. Yang, and Z. Zhang, “Galvanometer driven optical system for laser dynamic focusing,” *Opt. Express*, vol. 31, no. 1, p. 673, Jan. 2023, doi: 10.1364/OE.476921.

[49] R. Zmijan *et al.*, “High throughput imaging cytometer with acoustic focussing,” *RSC Adv.*, vol. 5, no. 101, pp. 83206–83216, 2015, doi: 10.1039/C5RA19497K.

[50] H. Mikami *et al.*, “Virtual-freezing fluorescence imaging flow cytometry,” *Nat Commun*, vol. 11, no. 1, Art. no. 1, Mar. 2020, doi: 10.1038/s41467-020-14929-2.

[51] A. R. Anwar, M. Mur, and M. Humar, “Microcavity- and Microlaser-Based Optical Barcoding: A Review of Encoding Techniques and Applications,” *ACS Photonics*, vol. 10, no. 5, pp. 1202–1224, May 2023, doi: 10.1021/acsphotonics.2c01611.

[52] Y. Li, Y. T. H. Cu, and D. Luo, “Multiplexed detection of pathogen DNA with DNA-based fluorescence nanobarcodes,” *Nat Biotechnol*, vol. 23, no. 7, pp. 885–889, Jul. 2005, doi: 10.1038/nbt1106.

[53] Y. Feng, A. K. White, J. B. Hein, E. A. Appel, and P. M. Fordyce, “MRBLES 2.0: High-throughput generation of chemically functionalized spectrally and magnetically encoded hydrogel beads using a simple single-layer microfluidic device,” *Microsyst Nanoeng*, vol. 6, no. 1, Art. no. 1, Nov. 2020, doi: 10.1038/s41378-020-00220-3.

[54] H. Q. Nguyen *et al.*, “Programmable Microfluidic Synthesis of Over One Thousand Uniquely Identifiable Spectral Codes,” *Adv Opt Mater*, vol. 5, no. 3, p. 1600548, Feb. 2017, doi: 10.1002/adom.201600548.

[55] C. Lin *et al.*, “Sub-micrometer Geometrically Encoded Fluorescent Barcodes Self-Assembled from DNA,” *Nat Chem*, vol. 4, no. 10, pp. 832–839, Oct. 2012, doi: 10.1038/nchem.1451.

[56] Z. Zhang *et al.*, “A high-throughput technique to map cell images to cell positions using a 3D imaging flow cytometer,” *Proceedings of the National Academy of Sciences*, vol. 119, no. 8, p. e2118068119, Feb. 2022, doi: 10.1073/pnas.2118068119.

[57] D. P. Hoffman *et al.*, “Correlative three-dimensional super-resolution and block face electron microscopy of whole vitreously frozen cells,” *Science*, vol. 367, no. 6475, p. eaaz5357, Jan. 2020, doi: 10.1126/science.aaz5357.

[58] F. J. Timmermans and C. Otto, “Contributed review: Review of integrated correlative light and electron microscopy,” *Rev Sci Instrum*, vol. 86, no. 1, p. 011501, Jan. 2015, doi: 10.1063/1.4905434.

[59] M. Schächtele, J. Kemmler, J. Rheinlaender, and T. E. Schäffer, “Combined High-Speed Atomic Force and Optical Microscopy Shows That Viscoelastic Properties of Melanoma Cancer Cells Change during the Cell Cycle,” *Advanced Materials Technologies*, vol. 7, no. 6, p. 2101000, 2022, doi: 10.1002/admt.202101000.

[60] R. K. G. Tank *et al.*, “Correlative Super-Resolution Optical and Atomic Force Microscopy Reveals Relationships Between Bacterial Cell Wall Architecture and Synthesis in Bacillus subtilis,” *ACS Nano*, vol. 15, no. 10, pp. 16011–16018, Oct. 2021, doi: 10.1021/acsnano.1c04375.

[61] I. Constantinou *et al.*, “Self-Learning Microfluidic Platform for Single-Cell Imaging and Classification in Flow,” *Micromachines (Basel)*, vol. 10, no. 5, p. 311, May 2019, doi: 10.3390/mi10050311.

[62] M. Sesen and G. Whyte, “Image-Based Single Cell Sorting Automation in Droplet Microfluidics,” *Sci Rep*, vol. 10, p. 8736, May 2020, doi: 10.1038/s41598-020-65483-2.

[63] A. Ahmad *et al.*, “On the robustness of machine learning algorithms toward microfluidic distortions for cell classification via on-chip fluorescence microscopy,” *Lab Chip*, vol. 22, no. 18, pp. 3453–3463, Sep. 2022, doi: 10.1039/D2LC00482H.

[64] L. E. Weiss *et al.*, “Three-dimensional localization microscopy in live flowing cells,” *Nat. Nanotechnol.*, vol. 15, no. 6, Art. no. 6, Jun. 2020, doi: 10.1038/s41565-020-0662-0.

[65] K. Hiramatsu *et al.*, “High-throughput label-free molecular fingerprinting flow cytometry,” *Sci Adv*, vol. 5, no. 1, p. eaau0241, Jan. 2019, doi: 10.1126/sciadv.aau0241.

[66] Q. Xiong *et al.*, “Magnetic nanochain integrated microfluidic biochips,” *Nat Commun*, vol. 9, p. 1743, May 2018, doi: 10.1038/s41467-018-04172-1.

[67] R. R. Svejdal, D. Sticker, C. Sønderby, J. P. Kutter, and K. D. Rand, “Thiol-ene microfluidic chip for fast on-chip sample clean-up, separation and ESI mass spectrometry of peptides and proteins,” *Analytica Chimica Acta*, vol. 1140, pp. 168–177, Dec. 2020, doi: 10.1016/j.aca.2020.09.062.

[68] J. Q. Zhang, C. A. Siltanen, L. Liu, K.-C. Chang, Z. J. Gartner, and A. R. Abate, “Linked optical and gene expression profiling of single cells at high-throughput,” *Genome Biol*, vol. 21, p. 49, Feb. 2020, doi: 10.1186/s13059-020-01958-9.

[69] N. Altemose, A. Maslan, C. Rios-Martinez, A. Lai, J. A. White, and A. Streets, “μDamID: A Microfluidic Approach for Joint Imaging and Sequencing of Protein-DNA Interactions in Single Cells,” *Cell Syst*, vol. 11, no. 4, pp. 354-366.e9, Oct. 2020, doi: 10.1016/j.cels.2020.08.015.

[70] K. Lane *et al.*, “Measuring Signaling and RNA-Seq in the Same Cell Links Gene Expression to Dynamic Patterns of NF-κB Activation,” *Cell Syst*, vol. 4, no. 4, pp. 458-469.e5, Apr. 2017, doi: 10.1016/j.cels.2017.03.010.

[71] R. J. Kimmerling *et al.*, “Linking single-cell measurements of mass, growth rate, and gene expression,” *Genome Biol*, vol. 19, p. 207, Nov. 2018, doi: 10.1186/s13059-018-1576-0.

[72] J. Lamanna *et al.*, “Digital microfluidic isolation of single cells for -Omics,” *Nature Communications*, vol. 11, 2020, doi: 10.1038/s41467-020-19394-5.

[73] S. T. Gebreyesus *et al.*, “Streamlined single-cell proteomics by an integrated microfluidic chip and data-independent acquisition mass spectrometry,” *Nature Communications*, vol. 13, 2022, doi: 10.1038/s41467-021-27778-4.

[74] N. Cermak *et al.*, “High-throughput measurement of single-cell growth rates using serial microfluidic mass sensor arrays,” *Nat Biotechnol*, vol. 34, no. 10, pp. 1052–1059, Oct. 2016, doi: 10.1038/nbt.3666.

[75] H. W. Kuhn, “The Hungarian method for the assignment problem,” *Naval Research Logistics Quarterly*, vol. 2, no. 1–2, pp. 83–97, 1955, doi: 10.1002/nav.3800020109.

[76] S. B. Needleman and C. D. Wunsch, “A general method applicable to the search for similarities in the amino acid sequence of two proteins,” *Journal of Molecular Biology*, vol. 48, no. 3, pp. 443–453, Mar. 1970, doi: 10.1016/0022-2836(70)90057-4.

[77] T. Laurell, F. Petersson, and A. Nilsson, “Chip integrated strategies for acoustic separation and manipulation of cells and particles,” *Chem Soc Rev*, vol. 36, no. 3, pp. 492–506, Mar. 2007, doi: 10.1039/b601326k.

[78] B. Diamond, “University Physics with Modern Physics [13th Edition] Young & Freedman.pdf czarina salgado Academia”, Accessed: Jul. 19, 2023. [Online]. Available: https://www.academia.edu/35622725/University_Physics_with_Modern_Physics_13th_Edition_Young_and_Freedman_pdf_czarina_salgado_Academia

[79] Z. Li *et al.*, “Hybrid Nanoimprint−Soft Lithography with Sub-15 nm Resolution,” *Nano Lett.*, vol. 9, no. 6, pp. 2306–2310, Jun. 2009, doi: 10.1021/nl9004892.

[80] S. Hettiarachchi *et al.*, “Design and development of a microfluidic droplet generator with vision sensing for lab-on-a-chip devices,” *Sensors and Actuators A: Physical*, vol. 332, p. 113047, Dec. 2021, doi: 10.1016/j.sna.2021.113047.

APPENDIX A PROBABILITY CALCULATION

Given two sequences S_1 and S_2, which begin with a cell and end with a cell, and comprise respectively L_1 and L_2 beads, the probability of S_1 and S_2 being identical is given by:

$$P(S_1 = S_2) = \sum_{l=0}^{\infty} P(S_1 = S_2 | L_1 = L_2 = l) \cdot P(L_1 = l) \cdot P(L_2 = l)$$

Let us consider that the sequences are built iteratively, adding another object at every step until the next object is a cell, thus ending the sequence. Given the beads concentration $[beads]$ and the cell concentration $[cells]$, we assume that the probability of the next object randomly chosen being a bead is given by:

$$p_b = \frac{[beads]}{[beads] + [cells]}$$

Then, the probability for a sequence to be l beads long is given by:

$$P(L_{1/2} = l) = (1 - p_b) p_b^l$$

Finally, assuming that the different colors of beads are equally split among all the beads, the probability of two sequences of the same length being identical is given by:

$$P(S_1 = S_2 | L_1 = L_2 = l) = \left(\frac{1}{n_{colors}}\right)^l$$

With n_{colors} the number of bead colors.

Therefore, we can write:

$$\begin{aligned} P(S_1 = S_2) &= \sum_{l=0}^{\infty} P(S_1 = S_2 | L_1 = L_2 = l) \cdot P(L_1 = l) \cdot P(L_2 = l) \\ &= \sum_{l=0}^{\infty} \left(\frac{1}{n_{colors}}\right)^l \cdot \left((1 - p_b) p_b^l\right)^2 \\ &= (1 - p_b)^2 \sum_{l=0}^{\infty} \left(\frac{p_b^2}{n_{colors}}\right)^l \end{aligned}$$

$$P(S_1 = S_2) = \frac{(1 - p_b)^2}{1 - \frac{p_b^2}{n_{colors}}}$$

Using the concentration ratio $R = \frac{[beads]}{[cells]}$ so that $p_b = \frac{R}{R+1}$ and manipulating the equation, we get the result:

$$P = \frac{n_{colors}}{n_{colors}(R+1)^2 - R^2}$$